Contact Modelling for Forward Dynamics of Human Motion

by

Peter Brown

A thesis
presented to the University of Waterloo
in fulfillment of the
thesis requirement for the degree of
Master of Applied Science
in
Systems Design Engineering

Waterloo, Ontario, Canada, 2017

© Peter Brown 2017

I hereby declare that I am the sole author of this thesis. This is a true copy of the thesis, including any required final revisions, as accepted by my examiners.

I understand that my thesis may be made electronically available to the public.

Abstract

Multibody forward dynamics models of the human body are often used in predictive simulations of human motion. An important component of these models is contact modelling. For example, foot-ground contact plays a crucial role in obtaining accurate results from a walking or running simulation and contact models of joints are necessary to determine accurate joint pressures.

Contact models increase multibody system equation complexity (often dramatically) and can introduce nonlinearities and discontinuities into the system equations. This is particularly problematic in predictive simulations, which may determine optimal performance by running a model simulation thousands of times. A desirable contact model should be accurate enough to recreate physiological motion and contact pressures yet still efficient enough to use in an optimisation.

A suitable contact model for multibody biomechanics is volumetric contact modelling. Volumetric contact modelling is ideally suited for large, conforming contacts, as is found in biomechanic applications, and has relatively simple, analytical equations (provided the contact surfaces can be approximated as simplified shapes). Another advantage is that volumetric contact can be used to calculate contact pressure, which is difficult to do with simpler point-contact models. In this thesis, volumetric contact was used in two biomechanics models to test its applicability: an anatomical knee model with tibiofemoral contact and a foot-ground contact model.

The volumetric knee model was based on another knee model in the literature, with the contact model replaced with volumetric contact. The volumetric model ran faster than real-time and had similar contact forces to the original model. Further improvements are possible by using medical images to determine the contact geometry and including muscles in the model.

A friction model is an important part of some biomechanic contact models, particularly the foot-ground contact model. A literature review revealed that many current friction models introduce discontinuities into system equations or are unnecessarily complex. A novel continuous friction model was developed which uses a minimum number of parameters for easy parametrisation.

A novel, three-dimensional foot-ground contact model was developed and validated, for future use in a human gait simulation. The foot model used volumetric contact equations for ellipsoidal geometry (which were derived in this thesis, as an improvement on previous sphere-plane contact models). A gait experiment was used to parametrise and validate the model (except for the friction parameters). The model ran over 100 times faster than real-time (in an inverse simulation) and matched experimental normal force and centre of pressure location (with less than 7% root-mean-square error).

It was discovered that the designed gait experiment could not be used to determine the friction parameters for the foot-ground model. A possible alternative was suggested, and the validation of the friction portion of the model was left to a future study.

In conclusion, volumetric contact can be used to produce a computationally efficient and accurate contact model.

Acknowledgements

I would like to thank Dr. John McPhee, my supervisor, for providing the opportunity to do this work with him and for his advice and supervision.

I also thank everyone else in the Motion Research Group for their advice, help, and friendship during my years as a member of the group.

Additionally, I thank Dr. Stacey Acker and David Kingston of the Biomechanics of Human Mobility Lab for the use of their lab and for their assistance performing the human gait experiment.

Table of Contents

List of Figures

List of Tables

Chapter 1

Introduction

1.1 Human Motion Analysis

Multibody dynamics is a useful tool for human movement simulation. A human can be modelled as a complex mechanism, commonly using rigid bodies to represent body segments, simple kinematic joints to represent anatomical joints, active torque elements to represent muscle forces, and various contact models to represent external contacts (such as foot-ground contact) [1]. More complex models can be used for the components to increase accuracy; for example, a joint could be modelled including the contact, ligaments and muscles in a joint, rather than just using a simplified kinematic joint. The modelling method used for each component of the human model is generally a compromise between simplicity and accuracy; simpler models are easier to build and faster to simulate, but are less accurate in matching human motion, while more accurate models tend to be more complex to build and can result in slow, computationally inefficient models.

One common use of a multibody human model is measuring human motion to calculate the internal forces and strains that cannot be easily measured, such as the muscle forces and ligament strains. This is inverse dynamics. Another application of multibody models is forward dynamics simulation, or predictive simulation, in which a set of inputs (such as muscle forces) is used to simulate human motion. A forward dynamic model can be used in an optimisation routine with a physiological cost function to predict human motion in untested situations or to predict human movement optimised for certain criteria. Optimisation requires many simulations to converge to a solution (often thousands) so a computationally efficient model is needed, as well as an accurate one. Predictive simulation is currently an active area of research, and can be used for doctors seeking to predict consequences of therapy or surgery, trainers and sports specialists wanting to optimise athlete performance or equipment, and prosthesis designers wanting to optimise the equipment [1].

Some examples of current research in predictive human models include:

- models of total knee replacements, used to predict changes to lower limb kinematics, muscle loads, and ligament loads due to the replacement alignment [2], [3],

- full-body gait models, used to determine possible balance control and human energy optimisation methods [4], [5] or to predict new gait movements that limit knee contact loads [6],

- and models of athletes, used to predict optimal technique [7].

This list only serves as a sample of current research; there are many more uses of forward dynamic multibody models in human motion analysis.

1.2 Contact and Friction

One important aspect of biomechanic models is contact models. An accurate contact model is required to calculate joint contact forces and pressures, which may be used to determine the longevity of joint replacements [3], and to calculate ground reaction forces, which may be used to determine a gait pattern that reduces tissue stresses [8].

However, contact models introduce many challenges to modelling. Contact forces are often nonlinear, discontinuous, and result in stiff system equations. Contacts in biomechanics are often over large compliant surfaces (such as contact between the plantar surface of the foot and the ground, or between layers of cartilage in a joint). Detailed and accurate contact models tend to become increasingly computationally expensive, such as the foot contact model of Halloran et al., which took 99.5% of the computation time in a full-body gait simulation [8]. Simpler contact models are often based on point-contact models which are not accurate for conforming surfaces. A balance is needed between a simplified model that will be computationally efficient, and an accurate model.

Friction modelling, an important part of contact models, is another source of complexity and discontinuities in the system equations. Friction is generally ignored in human joint contact models, due to their low coefficient of friction, but it plays an important role in foot-ground contact and grasping of objects.

1.3 Objectives

The primary purpose of this thesis is to explore the potential use of volumetric contact in multibody biomechanics models. Volumetric contact, originally developed for contact modelling in robotics simulation [9], has several characteristics that are useful for multibody biomechanics. Volumetric contact considers pressure developed across the whole contact surface, making it more accurate for conforming geometries than point contacts and allowing the surface pressure to be calculated (unlike point contact models). Additionally, if the contact geometry is simplified to analytical shapes, the contact forces can be described using analytical equations, which results in a model more computationally efficient than finite element models or discrete elastic foundation models.

Two biomechanic models using volumetric contact are described in this thesis: a knee model and a foot-ground contact model.

To the author's best knowledge, volumetric contact has not been used in a human joint model before now. Volumetric contact has promising potential for joint contact since it can model large, conforming contact surfaces and can be used to determine contact pressure, which is a useful measure for determining comfort and osteoarthritis progression. A proof-of-concept knee model was created, based on another model in the literature, to determine if volumetric contact could make a computationally efficient model with similar accuracy to the original model in the literature.

Volumetric contact has been previously used in foot-ground contact models, but these have been limited to 2D contact and spherical geometry [10]. The work on foot-ground contact in this thesis had two primary objectives: to derive equations for volumetric contact of an ellipsoid and plane, since ellipsoids can match complex geometry more closely than spheres can, and to experimentally parametrise and validate a 3D foot model.

Current velocity-based friction models are also evaluated for use in multibody optimisation studies in this thesis. It is noted that many models have discontinuities or needless complexities, so a new model that is continuous, differentiable, computationally efficient, and uses few parameters (to aid in simplicity of parametrisation and use) is presented.

1.4   Document Structure

This thesis explores the use of volumetric contact modelling in multibody biomechanics applications. Some background to the topic of contact in biomechanics is provided in Chapter 1, and a more detailed literature review on contact and friction models is given in Chapter 2. A literature review of current knee modelling methods and foot-ground contact models is also given in Chapter 2.

Chapter 3 describes a basic knee model, which uses volumetric contact to model the tibiofemoral contact.

Chapter 4 describes some current velocity-based friction models, notes some of their shortcomings, and describes a novel continuous friction model to address these issues.

Chapter 5 contains a more developed use of volumetric contact with friction in a foot-ground contact model. This chapter is divided into several major sections. In Section 5.1, volumetric contact equations are derived for ellipsoid-plane contact. These are used together with the friction model in Chapter 4 to develop a 3D foot-ground contact model, described in Section 5.2. This model is parametrised and compared against gait experiments in Section 5.3.

Conclusions and recommendations from the thesis are given in Chapter 6.

Chapter 2

Literature Review

A review of contact models and friction models is provided in this chapter[1], with a focus on models for predictive forward dynamic simulations.

For forward dynamic simulations, optimal control methods are often used to predict system inputs or to improve results of a tracking problem [12]. When using optimal control methods, a system model that is computationally efficient and leads to non-stiff equations is advantageous since it can reduce the computational time for a simulation that may be run thousands of times before finding a global optimum. A model that provides a continuous response is also desirable in order to obtain a reasonable frequency response [13]. Certain optimisation methods make use of the derivatives of the system equations [12], so it is desirable to use equations that are continuous and differentiable to model the system. Sensitivity analysis, which may be used to assist optimal control, benefits from a system with differentiable equations [14]. System derivatives are also used in calculating the Jacobian matrix for multibody analysis and simulation. For these purposes, a contact or friction model should ideally be computationally efficient, continuous, and differentiable.

2.1 Contact Dynamics Modelling

Gilardi and Sharf [15] define two main types of contact studies: contact *dynamics* and contact *mechanics*. Studies that focus on the net forces, velocities, and impulses between two bodies (such as multibody dynamics) fall under contact dynamics. Contact mechanics focuses on stress and displacement distributions within the contact area (the focus of tribology).

Since the primary focus of human motion modelling is replicating accurate motion, contact *dynamics* is of primary interest. Contact dynamics models can be divided into discrete and continuous models [15]. Discrete (or impulse-momentum) models assume that contact occurs over a short time and that contact forces can be approximated as

---

[1]Parts of this chapter (primarily Section 2.2) and Chapter 4 (with adaptations) were originally published in the ASME Journal of Computational and Nonlinear Dynamics [11]. © ASME.

instantaneous impulses. Continuous contact models assume that the contact forces act continuously throughout impact. Despite being more computationally complex, continuous models are better suited for intermittent and continuous contact, multiple contacts, and flexible bodies [15], which are common in biomechanical systems. Several main types of continuous contact models will be described here. Figure 2.1 serves as an overview of most of the models discussed in this section.

2.1.1   Point Contact Models

Point contact models assume contact between two surfaces occurs at a single point. This ignores any effects of geometry around the contact patch and makes a relatively simple model. Point contacts work well if the contact area is small, but are less accurate if contact could be anywhere within a large area. Objects with a large contact area can be modelled using several point contacts spread over the contact area, but this increases model complexity.

One of the simplest point contact models with energy dissipation is the Kelvin-Voigt model (Figure 2.1a), which represents the contact forces as a parallel spring and dashpot:

$$F_n = k\delta + d\dot{\delta} \tag{2.1}$$

where F_n is the normal contact force, k is the spring constant, d is the dashpot constant, and δ is the penetration or deformation depth. Note that this equation specifies the contact forces when contact exists (i.e. $\delta >= 0$); if there is no contact then $F_n = 0$. A concern with this model is that the transition between contact and non-contact conditions is discontinuous due to the use of a linear dashpot. The damping parameter may also result in a non-physical negative normal force during separation.

To overcome these issues, Hunt and Crossley [16] proposed a contact model based on a modified form of Hertz law (Figure 2.1b). Hertzian theory assumes that surfaces act like elastic half-spaces, and that the surfaces are non-conforming (that is, that the contact area is small relative to the curvature of the contact surface) [17]. In order to account for energy dissipation, Hunt and Crossley added a damping term that scaled with the depth of penetration:

$$F_n = k\delta^n + (b\delta^n)\dot{\delta} \tag{2.2}$$

where k and n are constants dependent on material properties and contact geometry and b is the damping coefficient. The Hunt-Crossley contact model has been used extensively in various applications. The main disadvantage is that it is based on Hertzian theory, and is not as accurate for conforming surfaces.

Flores et al. [18], [19] and Gonthier et al. [20] provide a more detailed overview of these models and some other point contact models with further details on energy dissipation and its relation to the coefficient of restitution.

(a)

Kelvin-Voigt
$F_n = k\delta + d\dot{\delta}$

(b)

Hunt-Crossley (Hertz)
$F_n = k\delta^n + (b\delta^n)\dot{\delta}$

(c)

Finite element
Partial differential equations for each element

(d)

Elastic foundation
Discrete force equation at each spring element

(e)

Volumetric
$F_n = k_V V(1 + a\dot{\delta})$
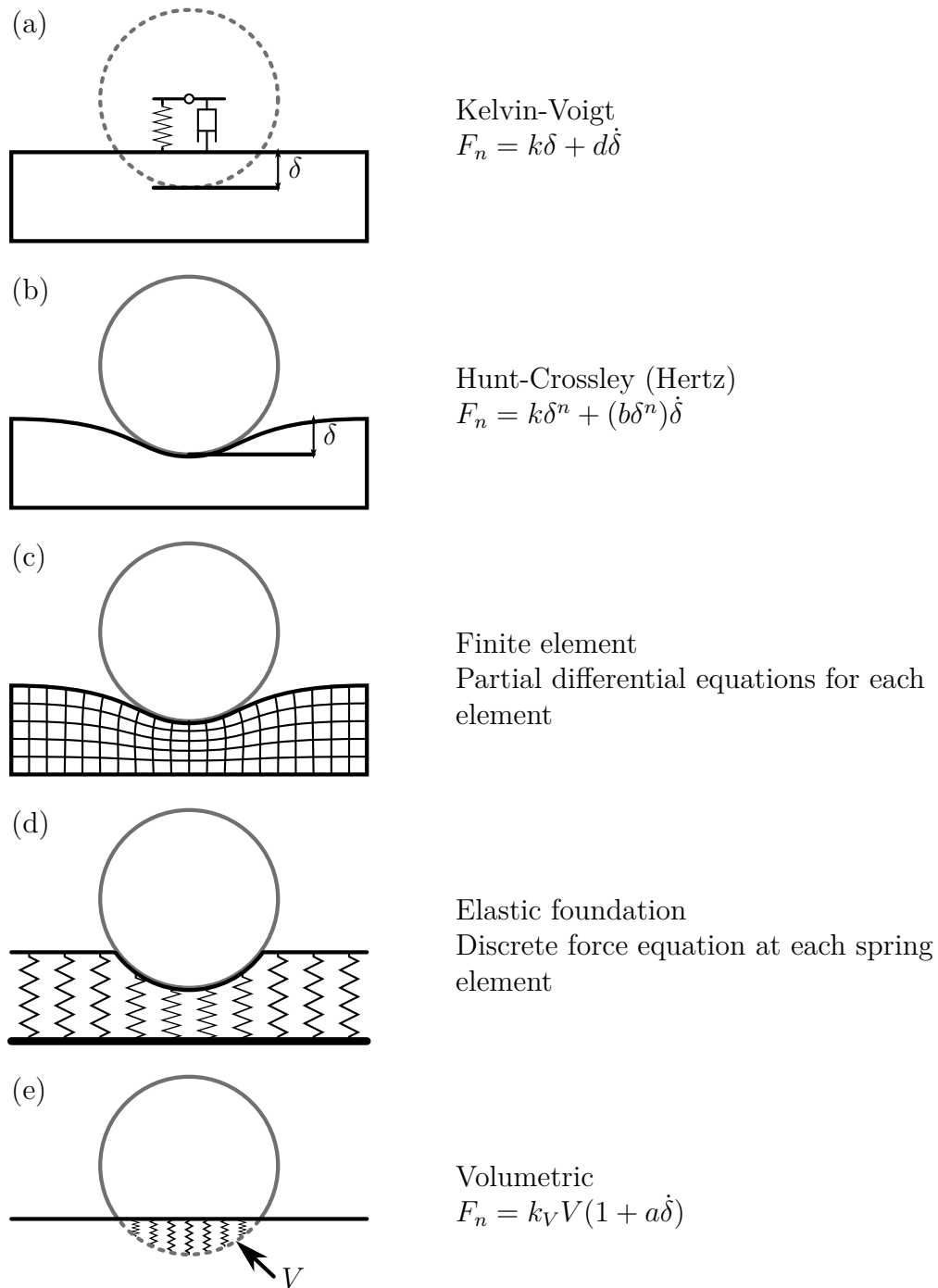
Figure 2.1: Overview of some contact models, their assumptions about the contact surfaces, and the contact force equations

2.1.2   Modified Point Contact Models

Some point contact models have been augmented by having some consideration for the surface geometry. The geometry of the contact surface—generally simplified to analytical shapes—is used to determine the primary location of contact across a large surface. Traditional point contact models can then be used at this point to determine the contact forces.

For example, Lopes et al. [21] used superellipsoids to represent foot geometry for a foot-ground contact model. The point of minimum distance between the superellipsoid and ground was used as the central point of contact and contact forces were calculated using an adapted Hunt-Crossley point contact model.

Millard and Kecskeméthy [22] used a disc in contact with a plane to represent foot-ground contact. A Hunt-Crossley model was used to calculate the contact forces at the point of minimum distance between the disc and the plane.

2.1.3   Finite Element Models

Finite element models [23] provide a much more detailed model of the stresses in the contact surface and can model complex shapes (Figure 2.1c). The mesh density of finite element models is the primary limitation on accuracy. However, the large computational cost of finite element models prevents them from easily being used in real-time applications or optimisation [24].

2.1.4   Elastic Foundation Models

In elastic foundation models, the contact surfaces are modelled as a layer of discrete springs over a rigid base (Figure 2.1d). This is less computationally expensive than finite element models and can be used to calculate the contact area and pressure. However, they are less accurate than finite element models since they do not consider sub-surface stresses or deformation of surrounding elements.

Elastic foundation models are generally based on discretising the contact surface into many springs. As a result, a large number of equations are generated for the system and it may become computationally expensive. Fregly et al. developed an elastic foundation based knee model they claim is sufficiently fast for some optimisation studies [25]; the usefulness of this model is likely dependent on the complexity of the rest of the model and the desired optimisation.

2.1.5   Surrogate Models

A computationally efficient alternative to finite element models and elastic foundation models are surrogate models [26], [27] which are computationally cheap models trained

to match results from a detailed model. Surrogate models are based on lookup tables rather than physics based models. Building a surrogate model requires significantly more work compared to other models since it requires a high-fidelity model to be built and then extensively tested to train the surrogate model. Another difficulty is that surrogate models are only valid over the conditions for which they have been trained, so they are not very flexible in their application.

2.1.6 Volumetric Contact Models

Volumetric contact is a more recently developed contact model, first proposed by Gonthier et al. for contact in robotic manipulators [9]. Volumetric contact is based on the elastic foundation model and models the surface as a continuous collection of tensile springs (Figure 2.1e).

Since volumetric contact considers pressure developed across the whole contact surface, it is more accurate than point contact models for complex and conforming geometries [28]. The contact forces can be found as an integral of the stresses developed across the contact area. If the contact geometry is represented as simplified shapes—which is generally done for volumetric contact—the distributed forces over the contact surface can be integrated to obtain analytical equations for the equivalent forces and torques at a resultant point. Volumetric contact additionally defines equations for rolling resistance, tangential friction, and spinning friction. This results in a set of equations much more efficient than discrete elastic foundation models, and not significantly more complex than point contact models.

Using volumetric contact, if the surface stiffness is linear, integration across the contact surface reveals that the normal force is directly proportional to the volume of penetration of the two surfaces. Similarly, the centre of pressure is at the centroid of this penetration volume, and all other contact forces can be related to the penetration volume and its properties [28], [29].

For a general case, the normal force equation for the volumetric contact model is

$$F_n = k_V V(1 + a v_{cn}) \tag{2.3}$$

where V is the volume of penetration, v_{cn} is the relative velocity of the two surfaces in the normal direction at the volumetric centroid, k_V is the volumetric stiffness, and a is the damping constant.

Volumetric contact is used and discussed further in Section 5.1.

2.2 Friction Modelling

Friction, the force that opposes the relative motion of two surfaces in contact, has been studied for more than 500 years, but there is still no conclusive method to model this phenomenon [13].

This section will be a review of simple friction models for multibody dynamics models and optimisation, not a detailed review of friction in general. For further details on sliding friction and its use in simulation, readers are directed to Berger's review paper [13]. More information about various types of friction, with a focus on tribology and numerical models, can be found in Zmitrowicz's survey paper [23].

2.2.1 Types of Friction Models

The most basic models for friction express the force of friction as a function of the normal force and the relative velocity of the surfaces. One of the earliest is the Coulomb friction model. This model can be given as

$$F_f = \mu F_n \, \text{sign}(v) \tag{2.4}$$

where F_f is the friction force, F_n is the normal force between the bodies, μ is the coefficient of friction, v is the relative velocity, and the sign function is described as

$$\text{sign}(x) = \begin{cases} -1 & x < 0 \\ 1 & x > 0 \end{cases} \tag{2.5}$$

A force-velocity curve for the Coulomb friction model is shown in Figure 2.2.
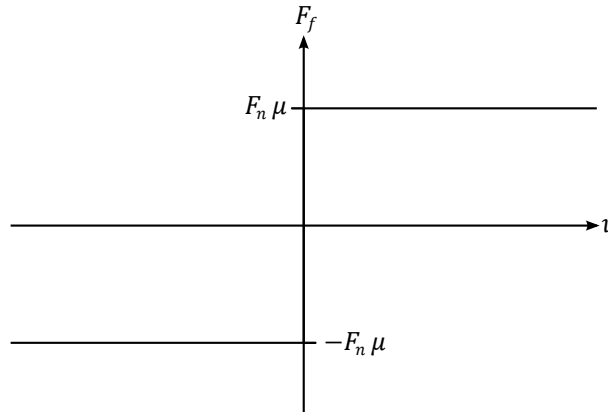
Figure 2.2: Coulomb friction model

The Coulomb friction model is rather basic and neglects the effects of velocity on friction, such as the Stribeck effect. The Stribeck effect describes the decrease in the force of friction experienced as the relative velocity between two surfaces increases (see Figure 2.3). In this thesis, the friction at or near zero velocity will be called static friction (or stiction), with a value of $\mu_s F_n$ (the static coefficient of friction multiplied by the normal force), and the friction experienced at higher velocities will be called dynamic friction (also commonly called Coulombic friction in other papers), with a value of $\mu_d F_n$ (the dynamic coefficient of friction multiplied by the normal force).
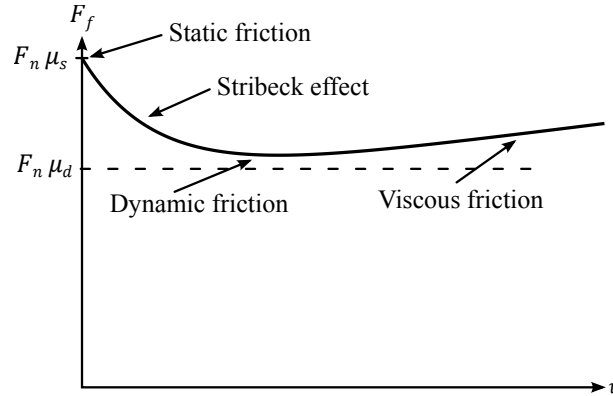
Figure 2.3: Velocity dependence of friction: Stribeck effect and viscous friction

For certain contacts, especially lubricated surfaces, friction also exhibits viscous characteristics. This effect will be called viscous friction, and is characterised by a linear increase in friction with respect to velocity (see Figure 2.3).

The model shown in Figure 2.3 causes problems in simulation and optimisation around $v = 0$, since the value of friction is discontinuous and undefined at this point. Most of the basic friction models can be described as different methods of handling this discontinuity.

One way to determine the value of friction at $v = 0$ is to set it equal to the applied force to satisfy static equilibrium conditions. However, this requires two different sets of equations for sticking and slipping conditions, and the system equations would have to be changed during simulation. This would cause a simulation or optimisation of the system to take longer to complete.

Instantaneous impact models, which are based on applying impulses within a discrete time-step, have been proposed to model friction as an alternative to a continuous friction model [30]. These models have good results for simulation, but are difficult to use for optimisation, so they are not explored here.

Another method to model friction is using a displacement-based or bristle friction model [20], [31], [32]. In these models an additional state variable tracks the displacement history, or bristle deformation, in order to calculate the friction forces. However, these models either do not consider the velocity dependence of friction [31] or in order to model it introduce discontinuities into the friction force [32] or become increasingly complex and require a large number of parameters [20]. Also, in displacement-based models, dynamic friction is often implemented as a saturation limit on the bristle deformation, which causes a discontinuity in the derivative of the state variable tracking bristle deformation.

The problems associated with discontinuities can be eliminated by using a continuous velocity-based equation that approximates the shape of the force-velocity curve in Figure 2.3. This can be done by assuming that the force of friction at zero velocity is equal to zero, and that the frictional force increases smoothly with an increase in velocity. This unfortunately introduces some other issues to the model—mainly that perfect "sticking" of two surfaces due to friction is not possible.

2.2.2 Continuous Normal Force

Since most friction models are a function of the normal contact force, the normal contact model must be continuous and efficient to ensure the friction model is as well (several contact models are described in Section 2.1). The Hunt-Crossley model or volumetric contact would meet these criteria.

2.2.3 Other Friction Phenomena

The friction models presented in this thesis neglect several known phenomena of friction such as time lag [13], micro-slip [33] (called pre-slip displacement by Berger [13]), and dwell-time dependence of friction [13]. Models describing these phenomena are more complex, often requiring additional states (such as bristle models, which are used to model micro-slip [34]), resulting in discontinuous equations, or have significantly reduced computational efficiency. Friction is also known to be affected by temperature, surface roughness, and wear debris [23], but including these effects would complicate models further. Due to their increased complexity and reduced efficiency, models that include these effects are not considered.

2.3 Knee Modelling

The knee, due to its importance in modelling human motion, has received much attention over the years. This literature review will be only a brief overview of knee modelling; for a more detailed literature review of the knee and knee modelling, the reader is directed to Madeti's review of knee biomechanics [35] and Hefzy's reviews of knee models [36], [37].

2.3.1 Phenomenological Models

Phenomenological knee models, as defined by Hefzy and Grood [36], [37], are models that have similar kinematics to the knee joint without considering the physiological components within the knee.

As an example, the simplest phenomenological model used is a revolute joint (or hinge joint), which approximates the main function of the knee (providing one axis of rotation) but does not model the tibiofemoral contact forces, ligament forces, or muscle forces. A revolute joint is often used to model the knee when the knee is not of primary interest in a model, such as in full-body models where the overall motion is of interest [5], [7], [38], [39]. However, a revolute joint does not capture the full kinematics of the knee and does not model the contact pressure or ligament forces.

A four-bar mechanism has also been used as a knee model [36] since the kinematics match those of a knee better than a revolute joint does. In a four-bar model, the four links represent the tibia, ACL, femur, and PCL. However, only the motion of the links has some

correspondence to their physiological counterparts; the forces in the links are unrelated. Another disadvantage with these models is that they are generally limited to 2D motion.

More complex mechanisms have been proposed that match knee motion more closely, such as the two 3D mechanisms by Di Gregorio et al. [40]. These mechanisms are comprised of several rigid links and ideal joints to form a single-degree-of-freedom system. Similarly, a single-degree-of-freedom equivalent kinematic joint can be used [41]; this joint uses a curve to represent any possible joint motion rather than using several links and joints.

The knee models mentioned up to now are of similar computationally efficiency to a revolute joint with various complexities of kinematics, but the kinematics only match one motion; the models do not consider the compliance of knee joint, such as that caused by joint cartilage compression and tendon elongation.

Though phenomenological models are useful in matching kinematics, they cannot be used to determine joint pressure in the knee.

2.3.2   Anatomical Models

Anatomical models [37] consider and model the anatomical components of the knee including the tibiofemoral surfaces and contact (bone, cartilage, and meniscus), the ligament forces, and the muscle forces. As a result, anatomical models are generally more complex and computationally expensive than phenomenological models, but provide a more complete and accurate model of the knee.

The modelling methods used in anatomical models has varied significantly. Contact has been modelled as rigid contact [42]–[45] or compliant contact [46], [47], contact surface geometry has been modelled as simplified 2D geometry (such as polynomials or splines) [42], [48]–[51] or 3D meshes [44], [45], [47], and the ligaments have been modelled using four [48], [50], [52] to 12 [43] elements.

A large number of knee models have been of a total knee replacement. These models have generally used the same modelling techniques—though the contact surface geometry may differ slightly—so these models will be presented together with natural knee models in the following sections of this review. Some total knee replacements have included an instrumented replacement [3], [47], [53], which can measure the internal contact forces that are difficult to obtain experimentally.

The remainder of this section will explore some of the details considered in anatomical knee models: the tibiofemoral contact model and geometry, the ligaments, and the muscles. This will describe some of the primary methods used to model these components and some of the advantages and disadvantages of these methods. A recurring theme is the need to find a balance between a model's complexity and accuracy and its simplicity and computational efficiency.

Tibiofemoral contact

A number of different contact models have been used in anatomical knee models to model the contact between the femoral condyles and tibial plateaus. The contact models mentioned in this section have previously been described in the contact review in Section 2.1.

Many early anatomical models used rigid contact [42]–[45]. While perhaps being more computationally efficient than other methods, rigid contact is a poor representation of the knee since it ignores cartilage and meniscus deformation. Blackevoort et al. [46] noted that compared to rigid contact, deformable contact models the conforming surfaces more accurately and is more numerically stable. An additional difficulty with rigid contact is that the contact pressure cannot be determined since force occurs at a single point.

A number of researchers [25], [46], [47], [54], [55] have used elastic foundation contact models, which assumes that the cartilage behaves as an elastic, compressible layer. This is much more accurate than rigid contact [46], but does not capture some material characteristics such as the incompressibility of cartilage. Adapted equations have been proposed to better model incompressible contact [56].

Finite element models have also been used to model contact [24], [57]. These model subsurface stresses, can model incompressible material, and are not confined to simple geometry. However, finite element models are too time consuming for simulating knee kinematics for real-time simulations [24], and certainly too complex for optimisation of activities.

A comparison of Hertz point contact, elastic foundation contact, and finite element contact modelling was done by Pérez-González et al. [24]. The elastic foundation model was found to be more accurate than the Hertz model, but its predictions were not as accurate as the finite element model. Since the computational efficiency of elastic foundation models was desirable (compared to finite element models) an adapted elastic foundation model was proposed by Pérez-González et al. to obtain results more similar to the finite element model.

Surrogate models of the knee have also been developed as a computationally cheap alternative to finite element models [26], [27]. Surrogate models must be trained by an anatomical model, but may be considered a phenomenological model since they do not consider the component functions (they act as lookup tables rather than a physics based model). Surrogate knee models have only been used to calculate the total joint force, not the contact pressure or ligament forces.

To the author's best knowledge, volumetric contact has not been used in joint models. This is likely due to how recently volumetric contact has been proposed compared to other contact modelling methods (in 2005 [9]). Volumetric contact is a promising method for use in human joint models in multibody simulations since it is better suited for large, conforming contact surfaces (compared to point contact models [28]), and is more computationally efficient than finite element models.

Tibiofemoral contact geometry

Contact geometry has been determined from cadaver studies or medical imaging of the bone and cartilage. Many models have only used the bone geometry, but DeFrate et al. [58] noted that cartilage geometry is also necessary to accurately determine contact location and pressures.

To simplify the system equations, the bone or cartilage geometry can be approximated as basic shapes (such as spheres [43] or polynomials [52], [55], [59]). This reduces the complexity of the system equations significantly, but also reduces the model accuracy. Accurate geometry is important, as it has been noted that knee models are most sensitive to contact geometry and ligament insertion locations [48].

In general, knee measurements have not been reused among researchers (possibly due to the complexity of sharing the data, and the desire to have subject-specific models), although some commonly recognised measurements now exist with the Grand Challenge Competition to Predict In Vivo Knee Loads [53] and human motion simulation packages such as OpenSim (from the National Center for Simulation in Rehabilitation Research). In fact, avoiding the reuse of measurements may be beneficial since subject-specific geometry can be important for model accuracy, as noted by Gerus et al. in a knee model [60] and Wesseling et al. in a hip model [61].

Ligaments

Various numbers of ligaments have been included in knee models, and various numbers of elements have been used to model each ligament. Ligaments are an important part of a knee model, but there are a number of difficulties in obtaining an accurate representation of ligaments.

Momersteeg et al. noted that ligaments have significantly different values of stiffness at different orientations and recommends using 4 to 7 linear elements in parallel per ligament to accurately capture the ligament properties [62], [63]. However, most models use fewer than 4 elements per ligament.

Ligament insertion sites are generally determined from medical imaging., though this may not be sufficiently accurate. Rachmat et al. discovered inter-observer differences in ligament placement could be considerable in a study using MRI scans of a knee [64].

Most models have not modelled the ligaments wrapping around the bones, though wrapping has been noted to change some ligament lengths by a noticeable amount [65].

The ligament force-strain relationship has generally been modelled as having two regions: an initial quadratic stiffness, followed by a linear stiffness [59]. This ignores some time-dependent properties of ligaments [66], but these likely only play a small role in regular human motion.

Ligament slack lengths are important to determine accurately due to the high stiffness of ligaments. Slack lengths may be obtained directly from some literature. Another method to determine ligament slack lengths relies on the fact that ligaments are close to their slack length at a particular knee position [52], [67].

Muscles

Muscles play an important role in stabilising the knee [68, p. 634] so muscles and muscle wrapping around the knee could be an important part of a complete knee model.

Many knee models ignore the contribution of muscles bridging the knee; in general these models were limited to replicating unloaded, passive motion and ligament strains [43], [48], [52], [59], [69]. Bersini et al. included just the quadriceps in their lower limb model [45], while other models included several muscles of the lower limb [44], [47], [49], [55], [70]–[72]. These models have been used to study gait, squatting, stepping, and other load-bearing movements.

2.4 Foot-Ground Contact Modelling

2.4.1 Contact Model

The contact modelling methods mentioned in this section are described in more detail in Section 2.1.

The simplest method of modelling the foot-ground interface is using an ideal joint (a fixed joint or revolute joint) [73], [74]. In these models, the foot contact must be modelled in several ways depending on the time-varying contact conditions: disconnected from the ground (during free-flight), fixed by a revolute joint to the ground (at the heel or toe, while the foot is in partial contact), or fixed entirely to the ground (when the foot is flat on the ground). The primary difficulty with this type of model is dividing the simulation into several phases (representing each contact condition) and handling each phase separately since each phase has a different set of equations. Another downside is that these models can produce unrealistic values for friction since slipping is not possible.

Another simple contact model is a rollover rocker [75], [76]. This is generally limited to two-dimensional motion of the foot. The contact surface is modelled as a curved rocker which rigidly contacts the ground at one point. This models the movement of the centre of pressure more accurately than an ideal joint, but is less accurate at heel-contact and toe-off and also requires separate phases of contact and non-contact conditions.

Continuous contact models are more accurate since they allow more movement during contact (such as slipping, rolling, or spinning as well as some compliance) and use the same set of equations for all contact conditions.

The most basic form of a continuous contact model is a point contact model. Point contact models of the foot use various numbers of point contacts (from 2 to 38) to represent the plantar surface [4], [77]–[80].

Modified forms of point contact models have also been used for foot-ground contact, including superellipsoid-plane contact by Lopes et al. [21] and disc-plane contact by Millard and Kecskeméthy [22] (previously mentioned in Section 2.1.2). According to Lopes et al.

[21], the superellipsoid-plane contact was more computationally efficient than a model comprised of a large number of point contacts with similar accuracy.

Finite element foot models have been used to calculate contact pressures [8], [81]. The model by Halloran et al. was incorporated into a multibody gait model which was optimised to minimise foot-ground contact pressure [8]. This model took over 10 days to solve with the finite element foot model requiring over 99.5% of the computation time, making it impractical for most applications.

Volumetric contact was first used in foot-ground contact by Millard et al. [79], who used a 2D two-segment foot model with three volumetric sphere-plane contact elements. This model was further developed by Sharif Shourijeh et al. who also proposed a hyper-volumetric model [10], [38]. Mouzo et al. used volumetric contact in a 2D foot model with a polynomial representing the contact surface [39]. Volumetric contact has yet to be used in a 3D foot model.

2.4.2 Foot Model

For forward dynamic analysis, the foot has been modelled as one [39], [79], two [4], [10], [22], [77]–[79], or three [21] independent rigid segments. A larger number of segments generally results in a model that is more accurate, but also a more computationally expensive model that requires additional actuators (for an active joint) or springs (for a passive joint) for the additional degrees of freedom.

The foot segments are generally joined by revolute joints which may be passively driven [10], [77], torque-driven [7], [22], or muscle-driven [4], [21].

Foot models for inverse dynamics or tracking experiments are often made of a larger number of rigid bodies—up to 8 [82]—but this type of model has not been used in a forward dynamic simulation, likely due to its complexity.

Chapter 3

Volumetric Contact Model of the Knee

The purpose of the work reported in this chapter was to develop a proof-of-concept volumetric contact knee model. This model was used to determine if a volumetric contact knee is effective in multibody dynamics for real-time simulations or optimisations.

A brief literature review of knee models is given in Section 2.3. Volumetric contact is considered for a knee model since it can accurately model a large, conforming contact area (as would be present in a joint) and is much simpler (and more computationally efficient) than finite element or elastic foundation models. Another reason to consider volumetric contact for a knee model is that it can be used to determine joint pressure (unlike point contact models). Joint pressure can be used in human movement optimisation and prediction [83]. To the author's best knowledge, this represents the first effort to use volumetric contact in a joint model.

Since the knee model developed in this chapter was a proof-of-concept to test volumetric contact, development was simplified by using another knee model in the literature as a basis. The model chosen for this purpose was a knee model by Abdel-Rahman and Hefzy [43], [84], which represented tibiofemoral contact as rigid contact between spheres and planes (representing the femoral condyles and tibial plateaus) and used 12 linear ligament elements (muscles were not included in the model). The model presented in this chapter was constructed the same as the model given by Abdel-Rahman and Hefzy, except with the rigid contact changed to volumetric contact. The model was validated only by comparing the simulation results to those in the literature.

3.1 Model Construction

The 3D anatomical knee model was created in the multibody simulation package MapleSim (2016. Maplesoft, Waterloo, ON, Canada). The knee geometry and ligament locations given by Abdel-Rahman and Hefzy [43] were used in this model, with the rigid contact being replaced with volumetric contact. The model is of the right knee. The age, weight,

and gender of the subject were not specified in [43], but the details are not crucial since this model only uses the knee geometry (the leg, foot, or body were not modelled).

Contact

Contact was modelled using a sphere-plane volumetric model, previously derived in [28]. This matches the geometry given in [43]. The geometry of the model is shown in Figure 3.1. The locations for the spheres representing the condyles and the planes representing the tibial plateaus were obtained from the equations in [43].
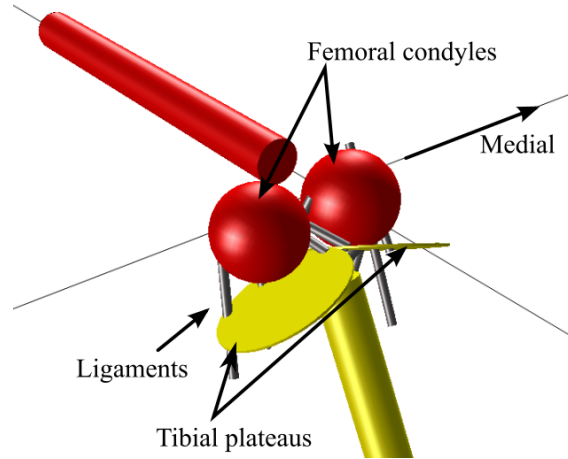
Figure 3.1: Volumetric knee model geometry and ligaments (right knee)

Only normal forces were considered in the contact model. Friction was ignored since friction is very low in synovial joints, and contact damping effects were ignored since large velocities were not expected. Also, these effects were not included in [43] and their inclusion would make a comparison between the two models less meaningful.

Ligaments

The same 12 ligament elements used by Abdel-Rahman and Hefzy were used in this model. These 12 elements (listed in Table 3.1 and shown in Figure 3.2) represented 7 primary ligaments in the knee. The ligament parameters used in the model are given in Table 3.2. Damping was added to the ligaments to reduce high-frequency responses as done by Guess [71] (0.5 Ns/mm).

The ligament force was a two-piece equation consisting of a quadratic "toe" region and a linear region:

$$F = \begin{cases} 0 & \epsilon \leq 0 \\ K_1 \left(L - L_0 \right)^2 & 0 \leq \epsilon \leq 2\epsilon_1 \\ K_2 \left[L - (1 + \epsilon_1)L_0 \right] & \epsilon \geq 2\epsilon_1 \end{cases} \tag{3.1}$$

where F is the ligament force, $\epsilon = \frac{L - L_0}{L_0}$ is the ligament strain, K_1 and K_2 are stiffness coefficients for the two regions, L is the current length, L_0 is the slack length, and ϵ_1 is

Table 3.1: List of used knee ligament elements and their shortened names

Ligament element	Short name
Anterior cruciate ligament, anterior fibres	ACL anterior
Anterior cruciate ligament, posterior fibres	ACL posterior
Posterior cruciate ligament, anterior fibres	PCL anterior
Posterior cruciate ligament, posterior fibres	PCL posterior
Medial collateral ligament, anterior fibres	MCL anterior
Medial collateral ligament, oblique fibres	MCL oblique
Medial collateral ligament, deep fibres	MCL deep
Lateral collateral ligament	LCL
Posterior capsule, medial	Posterior capsule medial
Posterior capsule, lateral	Posterior capsule lateral
Posterior capsule, oblique popliteal ligament	Oblique popliteal
Posterior capsule, arcuate popliteal ligament	Arcuate popliteal
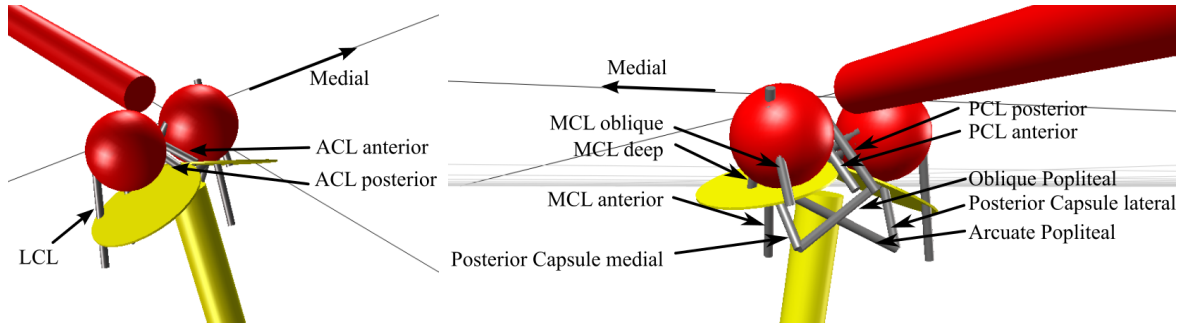
Figure 3.2: Ligament elements in knee model

the linear range threshold, specified as $\epsilon_1 = 0.03$. In order for the stiffness equation to be continuous, the stiffness coefficients, slack length, and linear range threshold must be related as follows:

$$L_0 = \frac{1}{4} \frac{K_2}{K_1 \epsilon_1}$$ (3.2)

Knee Measurement Convention

The tibiofemoral rotations and translations were measured using the conventions given by Grood and Suntay [85] (as was done by Abdel-Rahman and Hefzy). The rotation conventions are shown in Figure 3.3; exact definitions for the translations and rotations can be found in Grood and Suntay's paper [85].

Simulation

To compare the constructed volumetric contact knee model with the knee model by Abdel-Rahman and Hefzy, the same simulation described in [43] was recreated: with the knee

Table 3.2: Knee ligament element parameters (from [43])

Ligament element	Femoral attachment coordinates			Tibial attachment coordinates			K_1^{a}	K_2^{a}	L_0^{b}
	x (mm)	y (mm)	z (mm)	x' (mm)	y' (mm)	z' (mm)	(N/mm²)	(N/mm)	(mm)
ACL anterior	7.25	-15.6	21.25	-7.0	5.0	211.25	22.48	83.15	30.82
ACL posterior	7.25	-20.3	19.55	2.0	2.0	212.25	26.27	83.15	26.38
PCL anterior	-4.75	-11.2	14.05	5.0	-30.0	206.25	31.26	125.00	33.32
PCL posterior	-4.75	-23.2	15.65	-5.0	-30.0	206.25	19.29	60.00	25.92
MCL anterior	-34.75	-1.0	26.25	-20.0	4.0	171.25	10.00	91.25	76.04
MCL oblique	-34.75	-8.0	24.25	-35.0	-30.0	199.25	5.00	27.86	46.43
MCL deep	-34.75	-5.0	21.25	-35.0	0.0	199.25	5.00	21.07	35.12
LCL	35.25	-15.0	21.25	45.0	-25.0	176.25	10.00	72.22	60.18
Posterior capsule medial	-24.75	-38.0	6.25	-25.0	-25.0	181.25	12.00	52.59	36.52
Posterior capsule lateral	25.25	-35.5	8.25	25.0	-25.0	181.25	12.00	54.62	37.93
Oblique popliteal	25.25	-35.5	8.25	-25.0	-25.0	181.25	3.00	21.42	59.50
Arcuate popliteal	-24.75	-38.0	6.25	25.0	-25.0	181.25	3.00	20.82	57.83

[a] The values and units for columns K_1 and K_2 were mistakenly switched in [43].

[b] L_0 was not reported in [43], but could be determined from the values of K_1, K_2, and ϵ_1 using Equation (3.2).
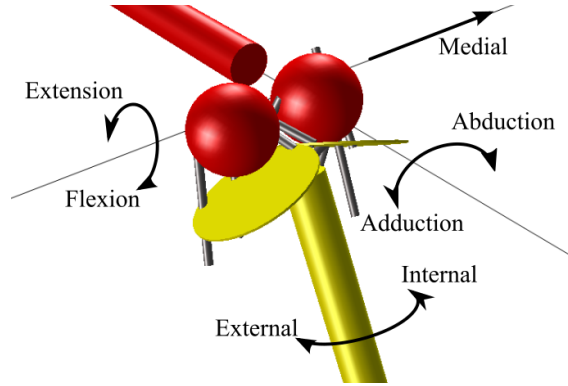
Figure 3.3: Right knee rotation conventions (the arrows indicate shank rotation relative to the femur)

starting fully extended and the longitudinal axis of the femur fixed horizontally (the anterior side facing up), an impulse was applied to the shank and the knee was allowed to flex to 90 deg (due to the force from the applied impulse and gravity). Gravity was not mentioned in [43], but the simulation results indicate that it was present in the simulation.

The volumetric stiffness was adjusted so that the peak normal force on the medial condyle matched the results in [43] (resulting in $k_V = 2 \times 10^9$ N/m^3). The moments of inertia of the femur and shank were not given in [43], so the mass (4 kg) was assumed to be distributed in a uniform density cylinder representing the shank. The cylinder geometry was adjusted so that the kinematics of the shank (specifically, the time for flexion to reach 90 deg) matched the results in [43] (resulting in a cylinder of 5 cm radius and 0.45 m length).

3.2 Results and Discussion

The simulation results are shown together with results from Abdel-Rahman and Hefzy's simulation in Figure 3.4 and Figure 3.5.

Due to the lack of readily available experimental results, the simulation was only compared to the simulation results of Abdel-Rahman and Hefzy's model [43], [84].

The trends of the knee contact forces for the medial and lateral condyles match reasonably well, including the lateral condyle normal force dropping to zero at 65 deg flexion. The flexion angle also matches well, but the other two rotations are of different magnitudes. The ligament forces vary significantly between the two models; none match exactly, but most have similar trends and overall magnitudes.

Some differences would be expected with this model due to the different contact models used and since the moment of inertia of the shank was estimated in this model (the value used by Abdel-Rahman and Hefzy [43], [84] was not reported). It is also possible that the ligament locations or slack lengths may have been slightly different (due to rounding errors) since it has been noted that knee models are very sensitive to these parameters [48].
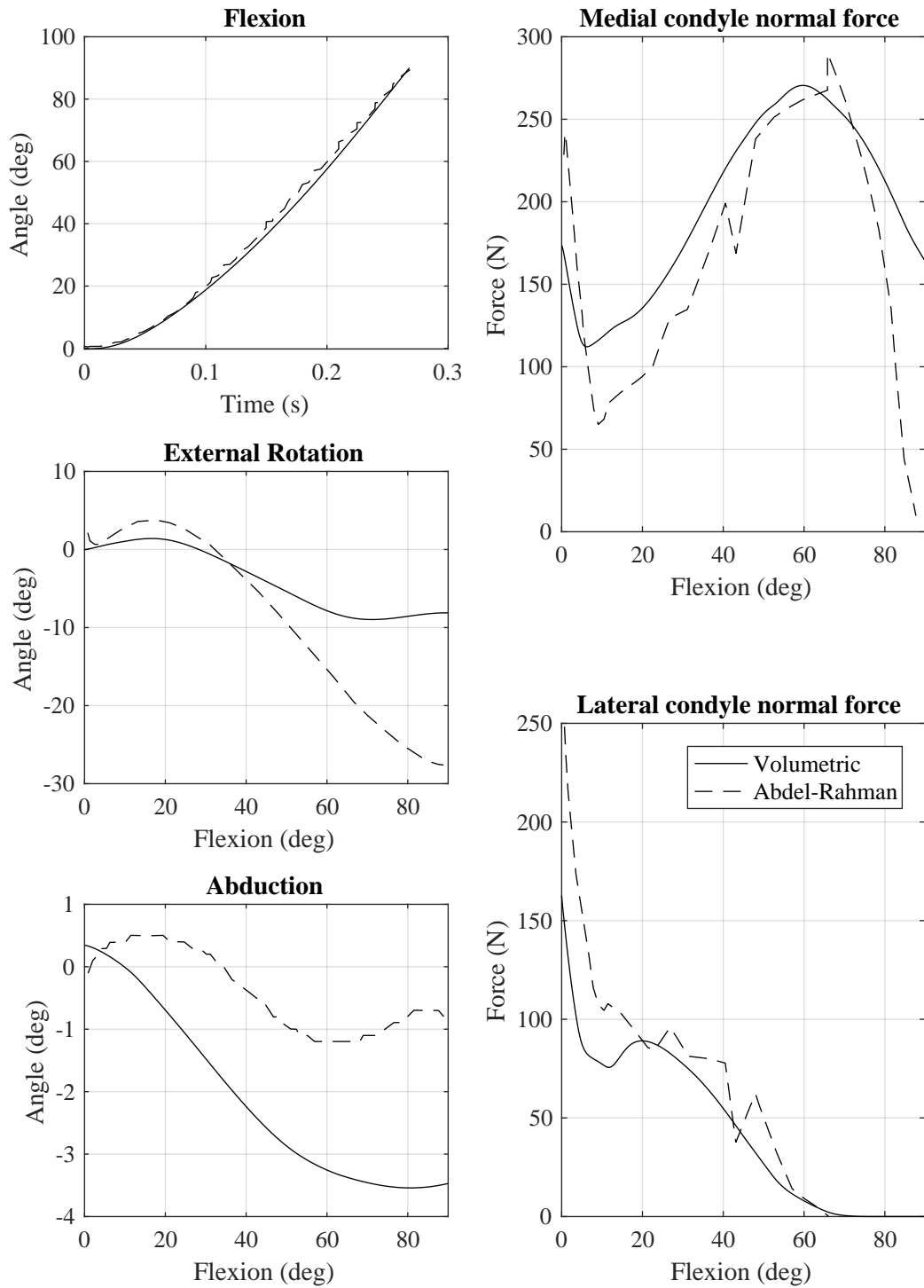
Figure 3.4: Simulated knee kinematics and normal contact forces
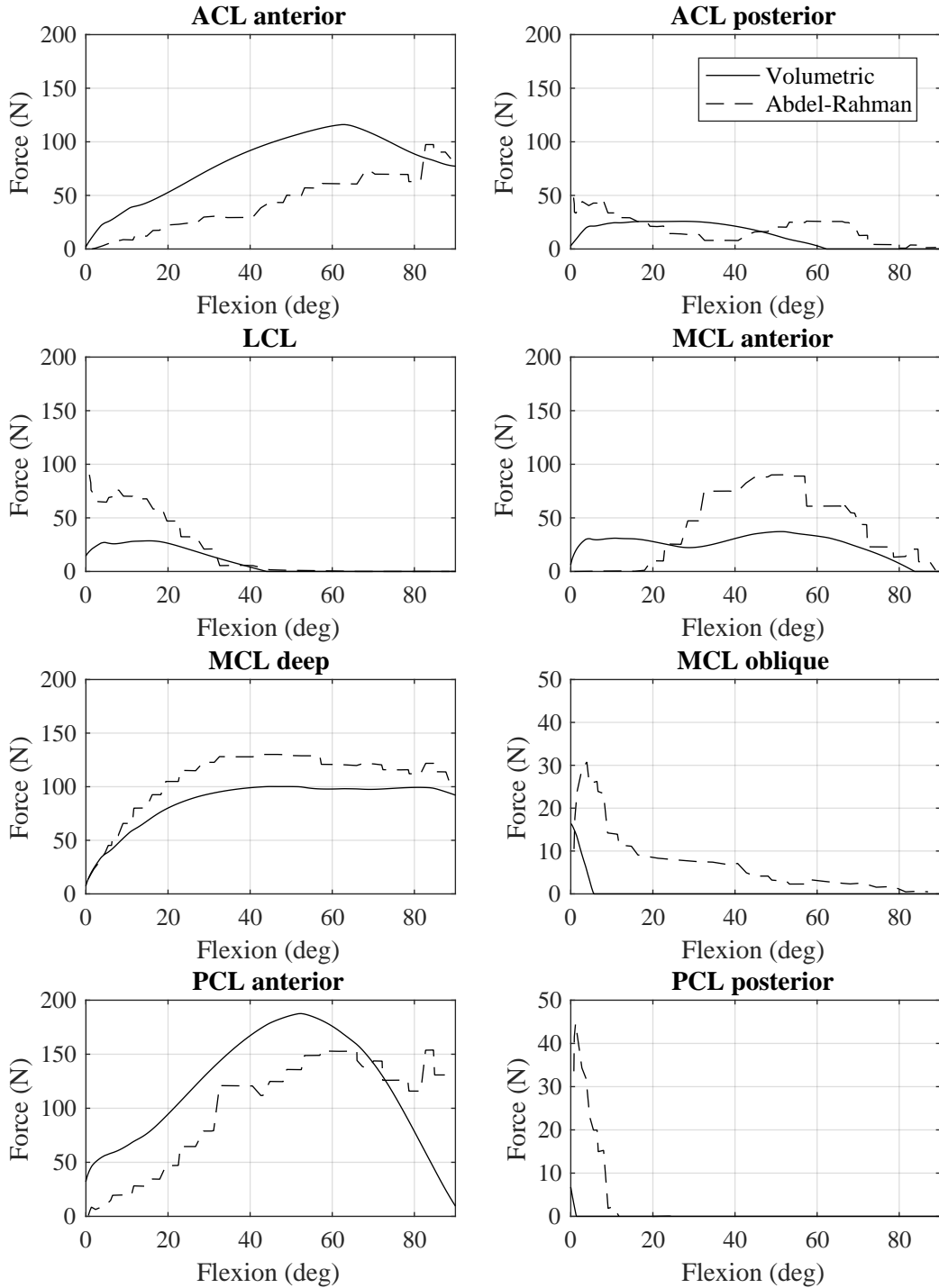
Figure 3.5: Simulated knee ligament forces

The simulation ran slightly faster than real-time (1.1 times faster) using a Rosenbrock solver with an error tolerance of 1×10^{-5} on a desktop computer (Intel® Core™ i7-3770 CPU @ 3.40GHz)

3.3   Conclusions and Recommendations

An anatomical knee model was designed with the tibiofemoral contact represented with a volumetric contact model. The model ran faster than real-time, and gave similar normal contact forces to the knee model of Abdel-Rahman and Hefzy [43], [84].

This model could be improved by using more recent knee measurements, rather than a relatively old model in the literature. Medical imaging techniques have improved since Abdel-Rahman and Hefzy's model was made, and more detailed measurements are readily available (such as from the Grand Challenge data [53]). To further improve the model, the contact surface could be modelled using shapes that more closely approximate the tibiofemoral contact geometry (such as ellipsoid-plane contact derived in Chapter 5 of this thesis). Knee models are very sensitive to this geometry [48]. Knee models are also sensitive to ligament placement [48], so more recent measurements for ligament insertion sites could improve the model fidelity. Including ligament wrapping could also improve the accuracy of the results.

Using subject-specific geometry could improve the model, as it has been noted to improve the accuracy of contact forces in the knee significantly [60].

The knee model could be further improved by including the patella and muscles since muscles play a role in stabilising the knee joint [68, p. 634].

Chapter 4

Continuous Friction Model

Friction is an important part of many dynamic systems, and, as a result, a good model of friction is necessary for simulating and controlling these systems. A literature review of friction modelling is given in Section 2.2. For optimal control applications, one of the primary concerns is having continuous and efficient system equations. For this purpose, velocity-based friction models (which are more likely to be differentiable, see discussion in Section 2.2) are most appropriate.

Unfortunately, many of the current velocity-based friction models have discontinuous equations. Three of these models are described in Section 4.1. To address this issue, a new model was developed and is presented in Section 4.2. This new model was designed to be continuous and differentiable, to be of similar efficiency to current models, and to have a small number of meaningful parameters to simplify model parametrisation[1].

4.1 Current Velocity-Based Friction Models

4.1.1 Andersson et al. Friction Model

One continuous model that describes the velocity dependence of friction was given by Andersson et al. [33]. This equation is shown below (variable names were changed for consistency throughout this chapter):

$$F_f = F_n \left[\mu_d + (\mu_s - \mu_d)e^{-(\frac{|v|}{v_s})^p} \right] \tanh(k_{\text{tanh}}v) + \mu_v v \tag{4.1}$$

where F_n is the normal force, v is the relative velocity, and μ_s, μ_d, and μ_v are the coefficients of static, dynamic, and viscous friction, respectively. The parameters v_s (the sliding speed coefficient) and p (an exponent) affect the shape of the decay from static to dynamic friction, while the parameter k_{tanh} (the tanh coefficient) determines the rate of increase

---

[1]The contents of this chapter and parts of Chapter 2 (with adaptations) were originally published in the ASME Journal of Computational and Nonlinear Dynamics [11]. © ASME.

from no friction at zero velocity to static friction. A typical force-velocity curve is shown in Figure 4.1. For comparison, the dotted line shows the friction-velocity plot without the smoothing provided by the tanh function or viscous friction (which is closer to the more realistic friction curve shown in Figure 2.3).

$$F_f = F_n \left[\mu_d + (\mu_s - \mu_d)e^{-\left(\frac{|v|}{v_s}\right)^p} \right]$$
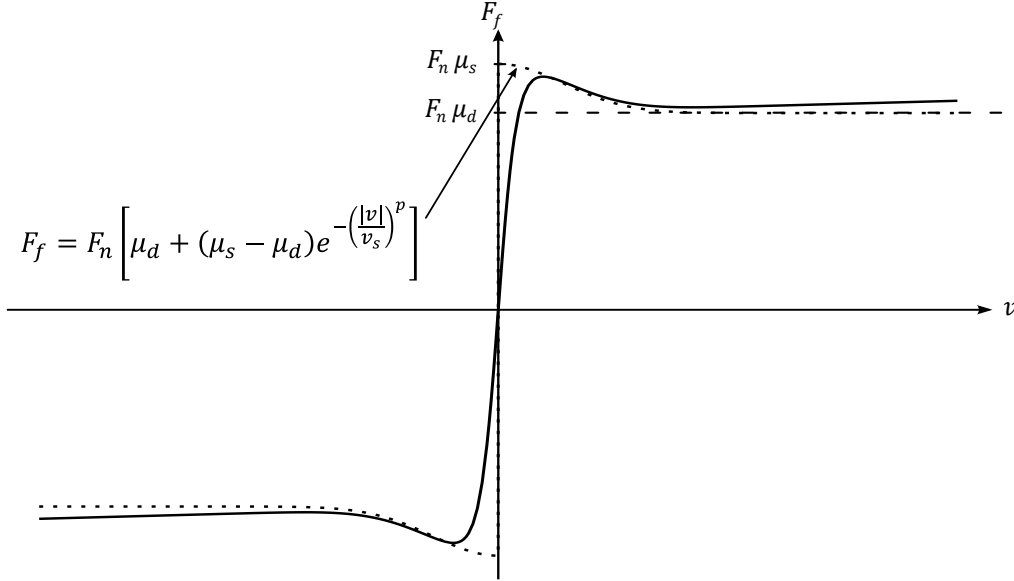
Figure 4.1: Andersson friction model

This model closely approximates the desired force-velocity curve while providing a smooth transition around $v = 0$, but there are some disadvantages with it. One disadvantage is that it is not obvious how some of the parameters affect the model or how they should be determined. This is particularly true of parameters v_s, p, and k_{tanh} which affect the shape of the force-velocity curve but have no obvious physical or practical meaning. Another difficulty with using this model is that if k_{tanh} is chosen poorly, the shape of the curve can change significantly: too small of a value can result in the initial peak in force (representing static friction) to be significantly less than the specified value $(F_n\mu_s)$ or to disappear completely.

As seen in Figure 4.1, the frictional force never reaches the specified value of static friction $(F_n\mu_s)$. This may result in a less realistic simulation, due to a mismatch with the real-world parameters. The value of μ_s could be increased to compensate for this, but that would complicate parameter identification.

Another difficulty with this model is that the viscous friction term must be enabled and disabled with contact (i.e. there is no smooth transition to enable viscous friction), which leads to discontinuous jumps in friction force whenever the surfaces collide with a non-zero tangential velocity.

4.1.2 Hollars Friction Model (Simbody)

Simbody uses the following friction model developed by Michael Hollars [86]:

$$F_f = F_n \left[\min \left(\frac{v}{v_t}, 1 \right) \left(\mu_d + \frac{2(\mu_s - \mu_d)}{1 + (\frac{v}{v_t})^2} \right) + k_v v \right] \tag{4.2}$$

where F_n is the normal force, v_t the transition velocity, and μ_s, μ_d, and k_v the coefficients of static, dynamic, and viscous friction, respectively (a different symbol is used for the coefficient of viscous friction since it has different units from the one used by Andersson). The min function returns the minimum of two values. A typical friction-velocity curve for the model is shown in Figure 4.2 (without viscous friction for clarity).
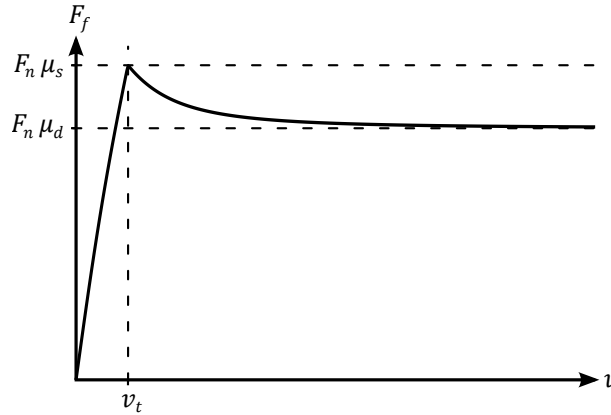
Figure 4.2: Hollars friction model

An advantage of this model is that v_t has a physical meaning: v_t specifies the point of maximum force representing static friction. Also, unlike Andersson's model, at v_t the value of friction reaches the known, specified value of static friction ($F_n \mu_s$).

A disadvantage with this model is the use of the min function, since it introduces a discontinuity to the equation at $v = v_t$ and is only valid for positive values of velocity. Also, the viscous friction implementation is unrealistic since it scales linearly with normal force; viscous friction should be independent of normal pressure [23]. This also means that the viscous friction coefficient, k_v, must be tuned according to the normal forces that are expected in the simulation for the results to match a more realistic viscous friction model (i.e. $k_v = \mu_v / F_{n\ ave}$, where $F_{n\ ave}$ is the average value of F_n during contact).

4.1.3 Specker et al. Friction Model

Specker et al. recently proposed a new approach for dynamic friction models [87]. The friction model given by Specker et al. is:

$$F_f = \left[F_n \mu_s - F_n \mu_d \tanh \left(\frac{v_t}{v_d} \right) - k_v v_t \right] \frac{v}{v_t} e^{-\frac{1}{2} \left(\frac{v}{v_t} \right)^2 + \frac{1}{2}} + F_n \mu_d \tanh \left(\frac{v}{v_d} \right) + \mu_v v \tag{4.3}$$

where F_n is the normal force, v_t is the transition velocity for stiction, v_d the "characteristic velocity for dynamic friction," and μ_s, μ_d, and μ_v the coefficients of static, dynamic, and viscous friction, respectively. Specker recommends that for the general case $v_t = 2v_d$.

The Specker force-velocity curve is shown in Figure 4.3 (without viscous friction).
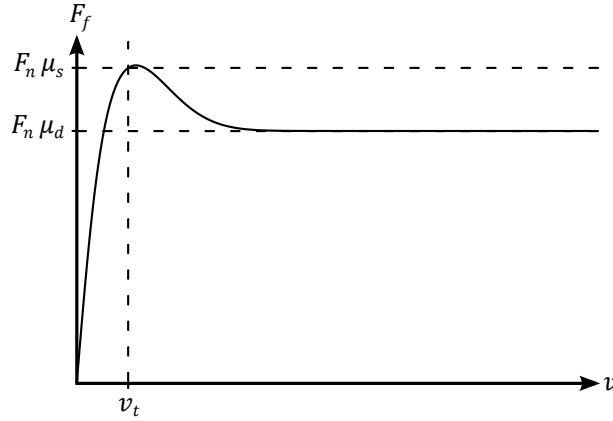
Figure 4.3: Specker friction model

It is uncertain why Specker recommends $v_t = 2v_d$, since this results in the peak in force occurring noticeably after v_t. Using $v_t = 2v_d$ results in the peak being at $v = 1.15v_t$ (for a general case where $\mu_d = 0.8\mu_s$ and $\mu_v = 0$). Using $v_t = 4v_d$ would seem more preferable, since it moves the peak to $v = 1.01v_t$. Furthermore, this change would result in the peak force being closer to $\mu_s F_n$. This difference is shown in Figure 4.4.
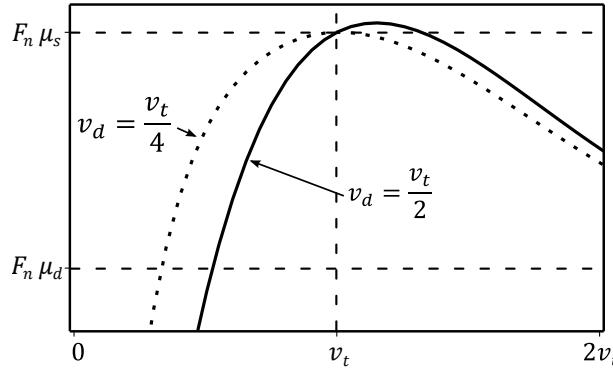
Figure 4.4: Choice of v_d in Specker's model

Overall, the use of v_d as an additional parameter lacks physical meaning and is not necessarily that useful. Having it as a separate parameter implies that it can be modified independently, but the relationship between v_t and v_d has an important effect on the starting shape of the force-velocity curve.

Similar to the friction model by Andersson et al. [33], the viscous friction in Specker's model is independent of normal force, which will create discontinuous jumps in friction force when surfaces collide with a non-zero tangential velocity.

4.2   Proposed Model

The following equation is proposed as a velocity-based model for friction force (F_f) which incorporates static, dynamic, and viscous friction, is valid for positive and negative values of velocity, and has physically meaningful parameters:

$$F_f = F_n \mu_d \tanh\left(4\frac{v}{v_t}\right) + F_n(\mu_s - \mu_d)\frac{\frac{v}{v_t}}{\left(\frac{1}{4}\left(\frac{v}{v_t}\right)^2 + \frac{3}{4}\right)^2} + \mu_v v \tanh\left(4\frac{F_n}{F_{nt}}\right) \tag{4.4}$$

where F_n is the normal force, v_t the transition velocity, F_{nt} the transition force, and μ_s, μ_d, and μ_v the coefficients of static, dynamic, and viscous friction, respectively.

The three summands in Equation (4.4) represent contributions of dynamic, static, and viscous friction, respectively. The contribution of the three terms to the force-velocity curve is shown in Figure 4.5. The dynamic friction term (representing Coulomb friction) quickly approaches $\mu_d F_n$ as the velocity increases from zero, and settles to within 0.1% of its final value by v_t. The static friction term (representing the stiction force and the Stribeck effect) has its maximum at v_t (similar to Hollars and Specker) with a value of $F_n(\mu_s - \mu_d)$, and then decays to zero for larger velocities where dynamic friction is the dominant factor. Motivated by previous observations in Specker's model, the model was designed to ensure a more precise match of static friction at v_t, for any choice of parameters.
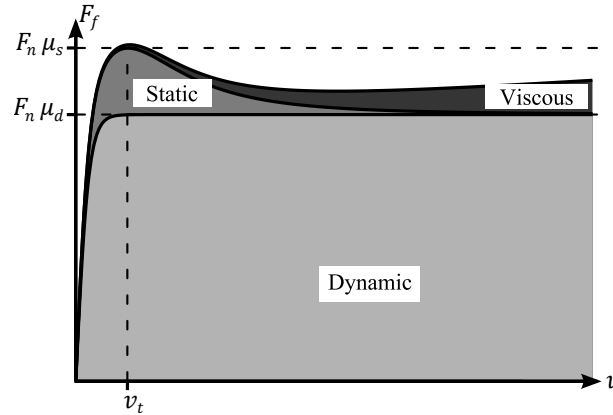
Figure 4.5: Force-velocity curve for proposed new friction model showing the contribution of the three summands (assuming $F_n \gg F_{nt}$)

The viscous friction term differs from the other two terms in that it does not scale linearly with normal force; instead, normal force is used to detect when to "enable" the viscous friction. This term physically corresponds to thin-film viscous friction, which scales linearly with velocity [13], [23]. The viscous friction term settles to within 0.1% of the true value (i.e. $\mu_v v$) when $F_n \geq F_{nt}$, where F_{nt} (the transition force) represents a minimum force expected between the surfaces for viscous friction to occur. Figure 4.6 shows how the dynamic and viscous friction terms scale with varying normal force (static friction is not shown, since it is negligible for $v \gg v_t$, but would scale linearly, the same as the dynamic
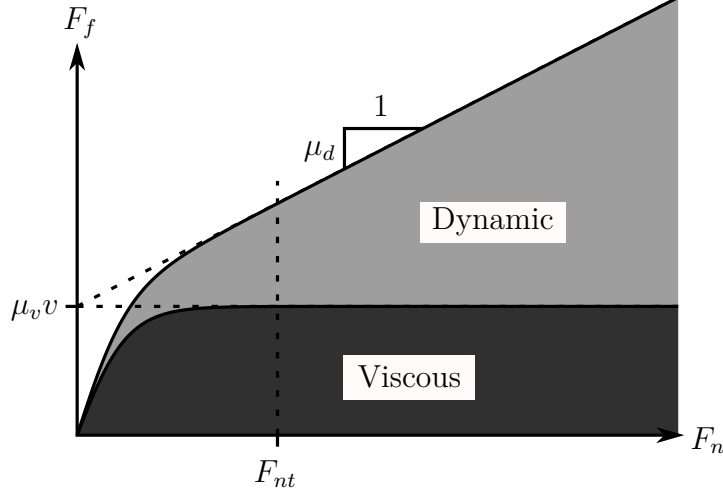
Figure 4.6: Friction force vs. normal force curve for proposed new friction model showing the contribution of the two summands (static friction is negligible) (assuming $v \gg v_t$)

friction term). The transition shown in Figure 4.6 would occur if two surfaces collide with a non-zero tangential velocity.

This model of viscous friction ensures that the frictional force has no discontinuities, provided that the normal force model is also continuous, and is a better model of viscous friction than scaling linearly with normal force.

If viscous friction is not required, then a simplified three-parameter friction model can be used:

$$F_f = F_n \mu_d \tanh\left(4\frac{v}{v_t}\right) + F_n(\mu_s - \mu_d)\frac{\frac{v}{v_t}}{\left(\frac{1}{4}\left(\frac{v}{v_t}\right)^2 + \frac{3}{4}\right)^2} \tag{4.5}$$

The number of parameters required to define the model was kept to a minimum, five when including viscous friction or three when not, while still capturing the phenomena of interest.

4.2.1 Derivative of System Equations

The friction force Equation (4.4) is a function of v and F_n. If both v and F_n are functions of some state variable q, then the analytical derivative of the friction force equation with respect to q is:

$$\begin{aligned}
\frac{\mathrm{d}F_f}{\mathrm{d}q} &= \frac{\frac{\mathrm{d}F_n}{\mathrm{d}q}(\mu_s - \mu_d)\frac{v}{v_t}}{\left(\frac{1}{4}\left(\frac{v}{v_t}\right)^2 + \frac{3}{4}\right)^2} + \frac{F_n(\mu_s - \mu_d)\frac{1}{v_t}\frac{\mathrm{d}v}{\mathrm{d}q}}{\left(\frac{1}{4}\left(\frac{v}{v_t}\right)^2 + \frac{3}{4}\right)^2} - \frac{F_n(\mu_s - \mu_d)\frac{v^2}{v_t^3}\frac{\mathrm{d}v}{\mathrm{d}q}}{\left(\frac{1}{4}\left(\frac{v}{v_t}\right)^2 + \frac{3}{4}\right)^3} \\
&\quad + \frac{\mathrm{d}F_n}{\mathrm{d}q}\mu_d \tanh\left(4\frac{v}{v_t}\right) + 4F_n\mu_d\frac{1}{v_t}\frac{\mathrm{d}v}{\mathrm{d}q}\left(1 - \tanh\left(4\frac{v}{v_t}\right)^2\right) \\
&\quad + \mu_v\frac{\mathrm{d}v}{\mathrm{d}q}\tanh\left(4\frac{F_n}{F_{nt}}\right) + 4\mu_v v\frac{1}{F_{nt}}\frac{\mathrm{d}F_n}{\mathrm{d}q}\left(1 - \tanh\left(4\frac{F_n}{F_{nt}}\right)^2\right)
\end{aligned} \tag{4.6}$$

This derivative can be used in the computation of the Jacobian matrix for multibody dynamic simulation, to support a system sensitivity analysis, or for formulating optimal control equations.

Unlike the other friction equations mentioned in this paper, the derivative of the proposed model is a continuous function with respect to v, F_n, and q. The derivative of Andersson's and Specker's friction models would be undefined at $F_n = 0$ (due to the viscous friction implementation), and the derivative of Hollars's model would have a discontinuity at $v = v_t$.

4.3   Simulations

As a demonstration, the proposed friction model and the Andersson, Hollars, and Specker friction models were used in two simulations: a classical stick-slip experiment (Rabinowicz [88]) and an impact experiment (Figure 4.7).
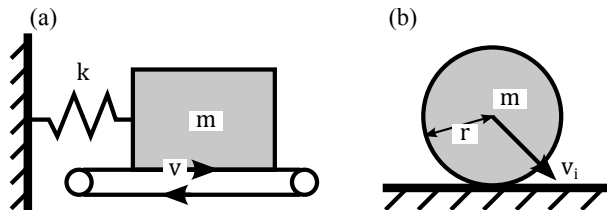
Figure 4.7: Setup of the stick-slip (a) and impact experiments (b)

The models were created and simulated using the simulation package MapleSim (2015. Maplesoft, Waterloo, ON, Canada), using the Rosenbrock solver with an error tolerance of 1×10^{-6}.

4.3.1   Stick-Slip Experiment

An experiment to test stick-slip motion, originally described by Rabinowicz [88], is shown in Figure 4.7a. A mass ($m = 1$ kg) attached to a spring ($k = 10$ N/m) is resting on a conveyor moving at a constant speed (0.1 m/s). The normal force is equal to the weight, mg, with $g = 9.81$ m/s^2. Since the stick-slip motion was of primary interest, viscous friction was ignored. The friction parameters for the proposed, Specker, and Hollars models were $\mu_d = 0.15$, $\mu_s = 0.2$, and $v_t = 0.001$ m/s. The additional parameters for Andersson's friction model were $v_s = 0.001$ m/s, $p = 2$, and $k_{\text{tanh}} = 10000$.

The simulation ran 3100, 3100, 2500, and 3100 times faster than real-time with the proposed, Specker, Hollars, and Andersson friction models, respectively. Results are shown in Figure 4.8.

The different friction models resulted in almost identical velocity profiles except for Andersson's model, which transitioned to slipping earlier. This is due to the earlier mentioned issue: that a poor choice of k_{tanh} can change the shape of the friction-velocity curve,
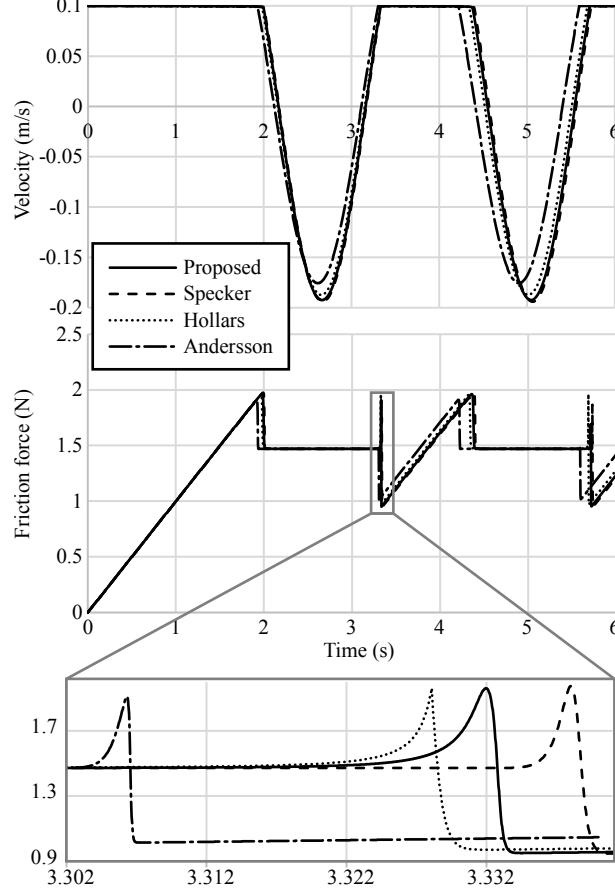
Figure 4.8: Mass velocity (top), friction acting on mass (middle), with slip-to-stick transition enlarged (bottom)

in this case by reducing the static friction coefficient. This problem could be alleviated by increasing k_{tanh}, but would result in stiffer system equations and slower simulations.

Also observable in Figure 4.8 is the C^1 discontinuity in Hollars's model at peak force; the other three models are C^1 continuous for this transition.

4.3.2 Impact Experiment

The impact experiment shown in Figure 4.7b consists of a sphere (mass of 0.5 kg, radius of 0.05 m, moment of inertia of $2/5mr^2$) striking a flat surface at a 45 degree angle with a velocity of 7 m/s. Gravity was neglected. To keep the focus of the model on the friction forces, a basic normal force model with no damping was used: $F_n = k\delta^2$, a C^1 continuous function, where δ is the surface penetration depth and k is the contact stiffness (set at 1×10^7 N/m^2). The friction parameters were the same as in the stick-slip experiment, with the addition of $\mu_v = 10$ Ns/m and $k_v = 0.0154$ s/m (chosen so that the different models predict the slip-to-stick transition at the same time).

The simulation ran 3.1, 2.7, 2.6, and 3.0 times faster than real-time with the proposed,

Specker, Hollars, and Andersson friction models, respectively. Contact first occurs at $t = 0$ and lasts for about 6.94 ms before rebound. Results are shown in Figure 4.9.
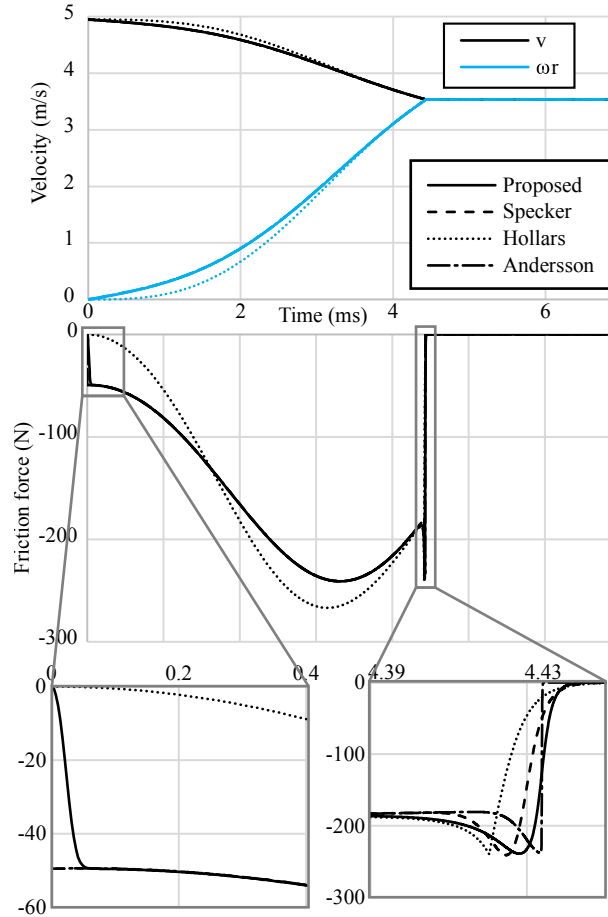
Figure 4.9: Horizontal velocity compared with the rotational velocity times the radius (top) and friction forces (middle) for the impact simulation

Since the ball has zero angular velocity prior to the impact, it slips for the first part of the contact and viscous friction plays a large role initially. Specker's and Andersson's models have a discontinuous jump at the initiation of contact due to the implementation of viscous friction, whereas the transition is smoothed for the proposed and Hollars's models. Hollars's model has a very different model of viscous friction, which results in a less realistic, though continuous, friction force curve (see previous discussion in Section 4.1.2). Identifying the viscous friction coefficient for Hollars's model is also more difficult since it needs to be tuned for the specific simulation (since it models friction as a function of normal force, which is not representative of true viscous friction behaviour, and the normal force experienced in an impact varies depending on impact conditions).

4.4 Discussion

The proposed model showed no C^0 or C^1 discontinuities in force, but the other three friction models did.

All four friction models had a similar computational cost, although Hollars's model stood out as being the slowest (the simulations took about 20% more time than the proposed model). The stick-slip simulation ran significantly faster than the impact experiment. This is probably due to the frequency of rapid transitions in frictional force in the latter simulation (the impact experiment had two major transitions in 6.94 ms, whereas the stick-slip experiment had two every 2.5 s).

4.5 Conclusion

A novel friction model that captures the effects of static, dynamic, and viscous friction while using a continuous, differentiable, computationally efficient equation has been proposed. The equation was designed to use physically meaningful parameters which are readily visible on a force-velocity or friction vs. normal force curve. The number of parameters was kept to a minimum—five with viscous friction, or three without—for simpler design. The proposed model avoids discontinuities while being of similar efficiency to other velocity-based models.

Since the model avoids discontinuities and is differentiable, it is well-suited to optimal control, sensitivity analysis, or multibody simulation applications.

Chapter 5

Volumetric Foot-Ground Contact

Accurate foot-ground contact models are necessary for modelling various types of human motion, especially gait. The purpose of the work reported in this chapter was to develop an accurate foot-ground contact model sufficiently simple and computationally efficient to use in forward dynamic models and optimisations. A review of current foot-ground modelling methods is in Section 2.4.

Volumetric contact has previously been used as an efficient contact model for foot-ground contact [38], [79], but was limited to 2D motion and the contact surface was approximated as spheres. However, the plantar surface is not perfectly spherical, so other geometry may provide more accurate results. To expand on spherical geometry, volumetric equations for ellipsoid-plane contact were derived (Section 5.1) and used in a 3D foot model (Section 5.2). This model was parametrised and validated using data from a gait experiment (Section 5.3).

5.1   Ellipsoid-Plane Volumetric Contact Model

The analytical equations for volumetric contact between an ellipsoid and a plane have not previously been developed. Previously derived equations for sphere-plane contact [28], [38], [79] will be used as a basis for ellipsoid-plane contact, with reference to Gonthier's detailed equations of volumetric contact [29].

5.1.1   Geometrical Values

Properties of sphere-plane contact

Contact equations for a generic sphere-plane contact will be used as a basis for the ellipsoid-plane equations. Let a unit sphere intersect a plane, where frame S is located at the centre of the sphere, $\vec{c}_S$ is the centroid of the volume of penetration, $\vec{p}_S$ is a point on the plane, $\hat{\mathbf{n}}_S$ is the normal of the plane (for ground contact, this vector would point upwards), and d is the depth of penetration (see Figure 5.1).
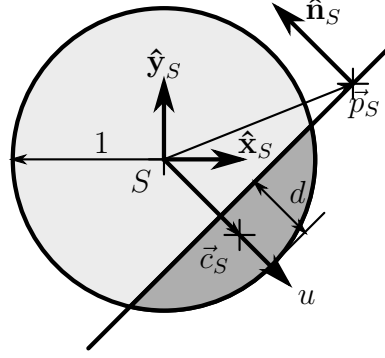
Figure 5.1: Sphere plane diagram

It is useful to define several properties based on the depth of penetration d:

$$d = 1 + \vec{p}_S \cdot \hat{\mathbf{n}}_S \tag{5.1}$$

For penetration distance d, the penetration volume can be defined as an integral of a revolution about the plane normal axis. Let a temporary u-axis point along $-\hat{\mathbf{n}}_S$ from the centre of the sphere, such that $r^2 = 1 - u^2$. The volume of penetration is:

$$
\begin{aligned}
V_S &= \int_{1-d}^{1} \pi r^2 \mathrm{d}u \\
&= -\frac{1}{3}\pi d^2(d-3)
\end{aligned}
\tag{5.2}
$$

Due to symmetry, the centroid must be along the u-axis.

$$\vec{c}_S = -c_S\hat{\mathbf{n}}_S \tag{5.3}$$

where

$$
\begin{aligned}
c_S &= \frac{1}{V_S}\int_{1-d}^{1} \pi r^2 u \mathrm{d}u \\
&= -\frac{3(d-2)^2}{4d-12}
\end{aligned}
\tag{5.4}
$$

Another property of interest for volumetric contact is the *weighted second moment of area* (weighted by the depth of penetration). This can also be thought of as the second moment of volume of the volume of penetration, with all the volume compressed into a single plane parallel with the contact surface. The perpendicular axis theorem [89, p. 241] applies this property: the second moment of volume about the plane normal axis must be equal to the sum of the second moment of volume for two perpendicular axes lying in the plane. Due to symmetry of the sphere-plane penetration volume, the second moment of volume for any axis lying in the plane must be equal and the second moment of volume about the plane normal is twice that of an axis tangential to the plane.

The weighted second moment of area about the plane normal can be defined as:

$$J_n = \int\limits_{1-d}^{1} \frac{1}{2}\pi r^4 \mathrm{d}u$$

$$= \frac{1}{30}d^3\pi(3d^2 - 15d + 20) \tag{5.5}$$

As mentioned before, the weighted second moment of area about an axis tangential to the plane would be half this amount:

$$J_t = \frac{1}{60}d^3\pi(3d^2 - 15d + 20) \tag{5.6}$$

Sphere-ellipsoid conversion

To find the geometrical properties for an ellipsoid, assume that the sphere is stretched along all three axes to form an ellipsoid; by a factor of a along the x-axis, b along the y-axis, and c along the z-axis (Figure 5.2).

To convert these values to that for an ellipsoid, have an equivalent, scaled frame E at the centre of the ellipsoid where

$$x_E = ax_S \tag{5.7}$$
$$y_E = by_S \tag{5.8}$$
$$z_E = cz_S \tag{5.9}$$

Note that in Figure 5.2 $\hat{\mathbf{n}}_E$ is not the scaled version of $\hat{\mathbf{n}}_S$, but the normal of the scaled plane.

Then the point on the plane in frame E can be related to the same point in frame S as:

$$\vec{p}_E = \mathbf{S}\vec{p}_S \tag{5.10}$$

where $\mathbf{S}$ defines a 'stretch matrix' for the frame transformation:

$$\mathbf{S} = \begin{bmatrix} a & 0 & 0 \\ 0 & b & 0 \\ 0 & 0 & c \end{bmatrix} \tag{5.11}$$

Since the plane has been stretched, the direction of the plane normal vector would be changed by the inverse of the stretch matrix:

$$\hat{\mathbf{n}}_E = \frac{\mathbf{S}^{-1}\hat{\mathbf{n}}_S}{|\mathbf{S}^{-1}\hat{\mathbf{n}}_S|} \tag{5.12}$$

Similarly,

$$\hat{\mathbf{n}}_S = \frac{\mathbf{S}\hat{\mathbf{n}}_E}{|\mathbf{S}\hat{\mathbf{n}}_E|} \tag{5.13}$$
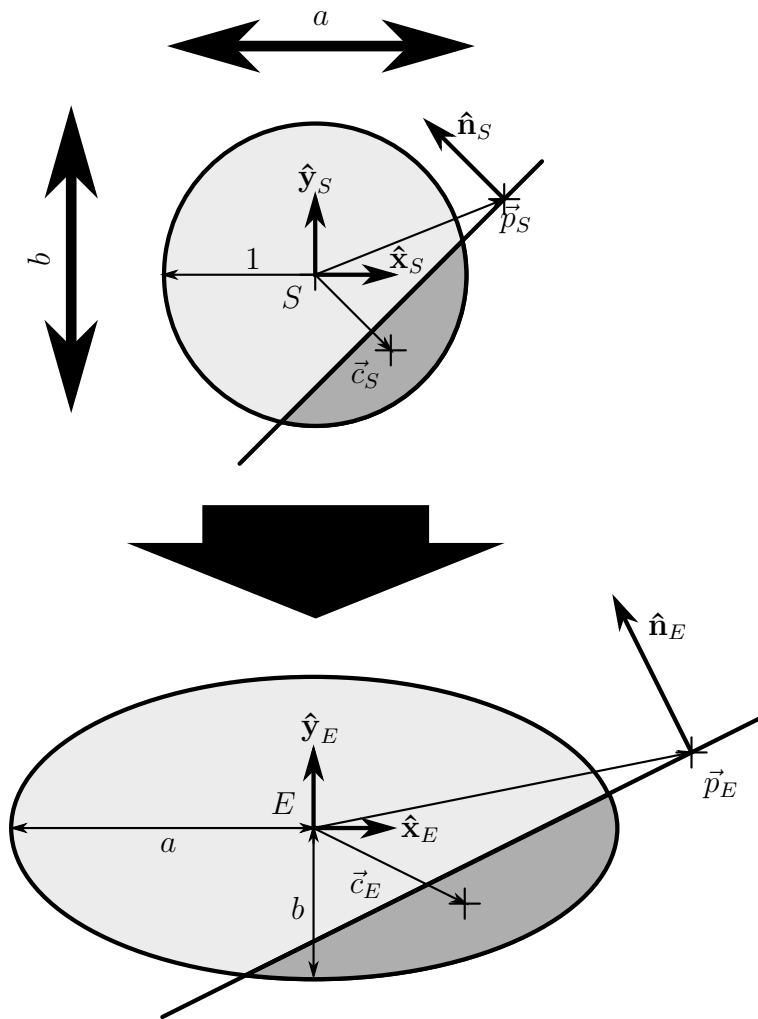
Figure 5.2: Sphere scaled to ellipsoid

Penetration volume and centroid

The penetration volume for the sphere has already been defined in Equation (5.4). The volume may also be defined as a triple integral:

$$V_S = \iiint\limits_V \mathrm{d}x_S \mathrm{d}y_S \mathrm{d}z_S \tag{5.14}$$

where V represents the volume of penetration. For the ellipsoid:

$$V_E = \iiint\limits_V \mathrm{d}x_E \mathrm{d}y_E \mathrm{d}z_E$$

Substitute Equations (5.7)–(5.9) to relate the volume of penetration of an ellipsoid to that of a unit sphere (Equation (5.14)):

$$V_E = \iiint\limits_V a\mathrm{d}x_S b\mathrm{d}y_S c\mathrm{d}z_S$$

$$= abc \iiint\limits_V \mathrm{d}x_S \mathrm{d}y_S \mathrm{d}z_S$$

$$V_E = abcV_S \tag{5.15}$$

Thus, the volume of of penetration for an ellipsoid is the scaled volume of penetration of a sphere.

Similarly, the centroid of penetration can be related using the basic definition of the centroid of volume:

$$\vec{c}_S = \frac{1}{V_S} \begin{bmatrix} \int\limits_V x_S \mathrm{d}V_S \\ \int\limits_V y_S \mathrm{d}V_S \\ \int\limits_V z_S \mathrm{d}V_S \end{bmatrix} \tag{5.16}$$

In frame E:

$$\vec{c}_E = \frac{1}{V_E} \begin{bmatrix} \int\limits_V x_E \mathrm{d}V_E \\ \int\limits_V y_E \mathrm{d}V_E \\ \int\limits_V z_E \mathrm{d}V_E \end{bmatrix}$$

$$= \frac{1}{abcV_S} \begin{bmatrix} \int\limits_V ax_S abc\mathrm{d}V_S \\ \int\limits_V by_S abc\mathrm{d}V_S \\ \int\limits_V cz_S abc\mathrm{d}V_S \end{bmatrix}$$

$$= \frac{1}{V_S} \begin{bmatrix} a\int\limits_V x_S \mathrm{d}V_S \\ b\int\limits_V y_S \mathrm{d}V_S \\ c\int\limits_V z_S \mathrm{d}V_S \end{bmatrix}$$

$$\vec{c}_E = \mathbf{S}\vec{c}_S \tag{5.17}$$

Second moment of contact area

To determine the equivalent weighted second moment of area for an ellipse, first consider an arbitrary second moment of volume matrix:

$$\mathbf{J} = \begin{bmatrix} J_{xx} & J_{xy} & J_{xz} \\ J_{xy} & J_{yy} & J_{yz} \\ J_{xz} & J_{yz} & J_{zz} \end{bmatrix} \tag{5.18}$$

where:

$$J_{xx} = \iiint (y^2 + z^2)\mathrm{d}V \tag{5.19}$$

$$J_{yy} = \iiint (x^2 + z^2)\mathrm{d}V \tag{5.20}$$

$$J_{zz} = \iiint (x^2 + y^2)\mathrm{d}V \tag{5.21}$$

$$J_{xy} = -\iiint xy\mathrm{d}V \tag{5.22}$$

$$J_{xz} = -\iiint xz\mathrm{d}V \tag{5.23}$$

$$J_{yz} = -\iiint yz\mathrm{d}V \tag{5.24}$$

A property that may be noted from Equations (5.19)–(5.21) is that:

$$\iiint x^2\mathrm{d}V = \frac{1}{2}\left(J_{yy} + J_{zz} - J_{xx}\right) \tag{5.25}$$

$$\iiint y^2\mathrm{d}V = \frac{1}{2}\left(J_{xx} + J_{zz} - J_{yy}\right) \tag{5.26}$$

$$\iiint z^2\mathrm{d}V = \frac{1}{2}\left(J_{xx} + J_{yy} - J_{zz}\right) \tag{5.27}$$

If an object with second moment of volume $\mathbf{J}$ were to be stretched, by a factor of a along the x-axis, b along the y-axis, and c along the z-axis then the new value for J_{xx} is:

$$J'_{xx} = \iiint ((by)^2 + (cz)^2)\mathrm{d}(abcV)$$
$$= (abc)\left(b^2 \iiint y^2\mathrm{d}V + c^2 \iiint z^2\mathrm{d}V\right)$$

using Equations (5.26) and (5.27) to relate back to the elements of $\mathbf{J}$:

$$J'_{xx} = \frac{abc}{2}\left(b^2(J_{xx} + J_{zz} - J_{yy}) + c^2(J_{xx} + J_{yy} - J_{zz})\right) \tag{5.28}$$

Similarly

$$J'_{yy} = \frac{abc}{2}\left(a^2(J_{yy} + J_{zz} - J_{xx}) + c^2(J_{xx} + J_{yy} - J_{zz})\right) \tag{5.29}$$

$$J'_{zz} = \frac{abc}{2}\left(a^2(J_{yy} + J_{zz} - J_{xx}) + b^2(J_{xx} + J_{zz} - J_{yy})\right) \tag{5.30}$$

For the off-diagonal elements of **J**:

$$J'_{xy} = a^2 b^2 c J_{xy} \tag{5.31}$$

$$J'_{xz} = a^2 b c^2 J_{xz} \tag{5.32}$$

$$J'_{yz} = a b^2 c^2 J_{yz} \tag{5.33}$$

Equations (5.28)–(5.33) can be used to define the transformation to the second moment of volume matrix when any volume is scaled along all the x, y, and z-axes by factors of a, b, and c, respectively. Let this transformation be defined by the function "scale" where

$$\mathbf{J'} = \text{scale}(\mathbf{J}, a, b, c) \tag{5.34}$$

In order to transform the weighted second moment of area of the sphere to that of the ellipsoid, two more coordinate frames will be defined at the penetration volume centroid. Assume that there is a known coordinate frame for the plane in contact with the ellipsoid in frame E (frame PE), where the z-axis is perpendicular to the plane (parallel with $\hat{\mathbf{n}}_E$) (see Figure 5.3).
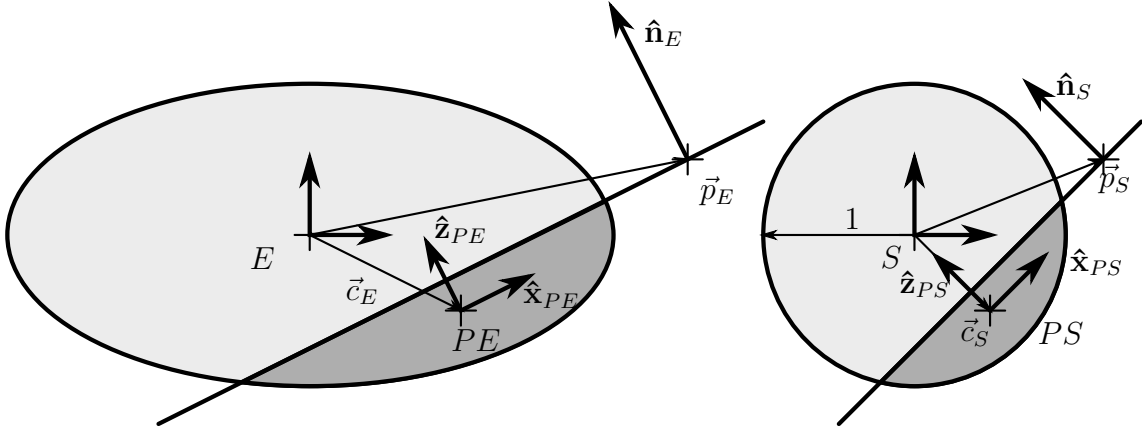
Figure 5.3: Sphere and ellipsoid contact with vectors for frame at centroid

Additionally, let there be a frame at the centroid of the sphere-plane volume, PS, with the z-axis parallel with $\hat{\mathbf{n}}_S$ and the x-axis along the transformed $\vec{x}_{PE}$ axis:

$$\hat{\mathbf{x}}_{PS} = \frac{\mathbf{S}^{-1}\hat{\mathbf{x}}_{PE}}{|\mathbf{S}^{-1}\hat{\mathbf{x}}_{PE}|} \tag{5.35}$$

The y axis is defined by the cross-product of the z and x axis.

With the coordinate frames fully defined, also let $\mathbf{R}_{PE}$ be the rotation matrix from frame PE to E, and $\mathbf{R}_{PS}$ from PS to S.

The weighted second moment of area for a sphere-plane contact has been defined for the normal and tangential axes (Equations (5.5) and (5.6)). This lines up with frame PS, and can be represented in a matrix:

$$\mathbf{J}_{PS} = \begin{bmatrix} J_t & 0 & 0 \\ 0 & J_t & 0 \\ 0 & 0 & J_n \end{bmatrix} \tag{5.36}$$

In order to transform this from frame PS to PE, the equivalent will be found in frame S (by finding the rotation), then scaled to frame E, and then rotated to frame PE:

$$\mathbf{J}_{PE} = \mathbf{R}_{PE}^T \, \text{scale} \left(\mathbf{R}_{PS} \, \mathbf{J}_{PS} \, \mathbf{R}_{PS}^T, a, b, c \right) \mathbf{R}_{PE} \tag{5.37}$$

Relative velocity

The relative velocity of the two bodies at the penetration volume centroid is also of interest for volumetric contact. See Figure 5.4 for frame and velocity definitions.
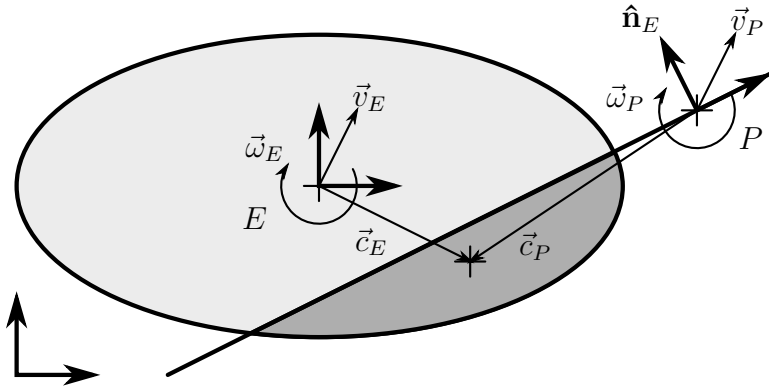
Figure 5.4: Sphere and ellipsoid contact relative velocity

The relative velocity of the two bodies at the centroid is:

$$\vec{v}_c = \vec{v}_E + \vec{\omega}_E \times \vec{c}_E - (\vec{v}_P + \vec{\omega}_P \times \vec{c}_P) \tag{5.38}$$

which can be divided into normal and tangential components:

$$\vec{v}_{cn} = (\vec{v}_c \cdot \hat{\mathbf{n}}_E)\hat{\mathbf{n}}_E \tag{5.39}$$
$$\vec{v}_{ct} = \vec{v}_c - \vec{v}_{cn} \tag{5.40}$$

The relative rotational velocity between the two bodies is:

$$\vec{\omega}_c = \vec{\omega}_E - \vec{\omega}_P \tag{5.41}$$

with components:

$$\vec{\omega}_{cn} = (\vec{\omega}_c \cdot \hat{\mathbf{n}}_E)\hat{\mathbf{n}}_E \tag{5.42}$$
$$\vec{\omega}_{ct} = \vec{\omega}_c - \vec{\omega}_{cn} \tag{5.43}$$

5.1.2 Contact Equations

Normal force

From Gonthier's derivations [29], the normal force for volumetric contact is:

$$\vec{F}_n = k_V V \left(1 + a_V |\vec{v}_{cn}|\right) \hat{\mathbf{n}}_E \tag{5.44}$$

where k_V is the volumetric stiffness and a_V is the damping coefficient. The other values (volume of penetration V and relative normal velocity $\vec{v}_{cn}$) were defined or derived in Section 5.1.1. For ellipsoid-plane contact, it is assumed that the plane would act as the contact surface.

Rolling resistance

Rolling resistance for volumetric contact is given as [29]:

$$\vec{\tau}_r = k_V a_V \mathbf{J} \vec{\omega}_{ct} \tag{5.45}$$

where $\mathbf{J}$ is the weighted second moment of area ($\mathbf{J}_{PE}$ in Section 5.1.1) and $\vec{\omega}_{ct}$ is the relative tangential angular velocity.

Tangential friction

Gonthier approximated tangential friction as follows [29]:

$$\vec{F}_t = F_n \mu \vec{v}_{ct} \tag{5.46}$$

where μ is a coefficient of friction, F_n the magnitude of the normal force, and $\vec{v}_{ct}$ the tangential relative velocity at the centroid.

In order to obtain a friction model that more closely matched dry friction and was still continuous with respect to velocity, the 3-parameter model presented in Chapter 4, Equation (4.5) was used. Incorporating that friction equation into Equation (5.46) resulted in the following model:

$$\vec{F}_t = F_n \, \mu(|\vec{v}_{ct}|) \frac{\vec{v}_{ct}}{|\vec{v}_{ct}|} \tag{5.47}$$

where

$$\mu(v) = \mu_d \tanh\left(4\frac{v}{v_t}\right) + (\mu_s - \mu_d)\frac{\frac{v}{v_t}}{\left(\frac{1}{4}\left(\frac{v}{v_t}\right)^2 + \frac{3}{4}\right)^2} \tag{5.48}$$

where μ_d is the dynamic coefficient of friction, μ_s the static coefficient of friction, and v_t the transition velocity.

Spinning friction

Gonthier's approximation for spinning friction is:

$$\vec{\tau}_s = \mu \frac{F_n}{V} \mathbf{J} \vec{\omega}_{cn} \tag{5.49}$$

Similar to tangential friction, this was adapted using the same friction model:

$$\vec{\tau}_s = \frac{F_n}{V} \mu(|\vec{\omega}_{cn}|) \mathbf{J} \frac{\vec{\omega}_{cn}}{|\vec{\omega}_{cn}|} \tag{5.50}$$

where

$$\mu(\omega) = \mu_d \tanh\left(4\frac{\omega}{\omega_t}\right) + (\mu_s - \mu_d)\frac{\frac{\omega}{\omega_t}}{\left(\frac{1}{4}\left(\frac{\omega}{\omega_t}\right)^2 + \frac{3}{4}\right)^2} \tag{5.51}$$

where ω_t the transition angular velocity.

Accuracy of friction equations

Note that these friction equations are an adaptation of an averaged integral. Due to simplifications, this friction model may not be accurate in all cases, such as when contact has a mixture of sticking and slipping or when a large amount of spinning is present. Also, the model does not have exact stiction (since it uses a velocity-based friction model) and does not capture the Contensou effect (since the tangential friction and spinning friction equations are decoupled). However, the model should be a good approximation for foot-ground contact which has a relatively short contact time, low surface velocities, and little spinning.

Equation manipulation

The equations defined in this section can be used to find the penetration volume, centroid, and weighted second moment of area of an ellipsoid-plane contact. These equations were expanded and simplified by using symbolic computing software Maple (2016. Maplesoft, Waterloo, ON, Canada). Due to the length and complexity of the equations, they will not be given here. All these equations were used to create a custom component model in MapleSim (2016. Maplesoft, Waterloo, ON, Canada) to use as part of the foot-ground contact model.

It was noted that the contact equations for the ellipsoid-plane model were significantly more complex that the sphere-plane contact model it was based on. In the author's opinion, it is likely that the equations for more complex shapes, especially those with less symmetry, will be even more complex or infeasible to determine analytically.

5.2 Foot Model

The foot-ground contact model was constructed in MapleSim. The foot model was made of two rigid segments: the foot segment (including the heel and ball of the foot) and the toe segment. The two segments were connected by a revolute joint representing the toe joint. The contact geometry was represented using several ellipsoids contacting the ground (using the ellipsoid-plane contact model developed in Section 5.1). Two ellipsoids were used to represent the foot segment, and one ellipsoid to represent the toe segment (as shown in Figure 5.5).
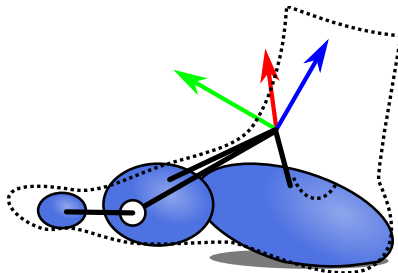
Figure 5.5: Foot model

The toe joint axis was defined as a line passing though the foot metatarsals 1 and 3.

For the initial model, to reduce complexity, the static friction term was ignored (i.e. $\mu_s - \mu_d = 0$). Also, the friction transition parameters were set to arbitrary low values: $v_t = 0.01$ m/s and $\omega_t = 0.01$ rad/s. All contacts were assumed to have the same volumetric stiffness and damping.

This resulted in a model with 30 parameters left to be determined; these parameters are listed in Table 5.1.

Table 5.1: Foot-ground contact model parameters to identify

Scope	Parameter(s)	Description	Units
	k_V	Volumetric stiffness	N/m^3
Global	a_V	Volumetric damping coefficient	s/m
	μ_d	Coefficient of friction	
Ellipsoid geometry (for each ellipsoid)	a, b, c	Dimensions	m
	r_x, r_y, r_z	Position	m
	α, β, γ	1-2-3 body-fixed Euler angles	rad

The MapleSim model was exported as C code and compiled in Matlab (R2016a. MathWorks, Natick, MA, USA) for use in an inverse dynamics optimisation.

5.3 Experimental Parametrisation

In order to parametrise and validate the foot model, a simple gait experiment was performed. Gait was chosen as it is one of the primary desired applications of the model.

5.3.1 Experimental Protocol

For the gait experiment, one participant (male, 24 yr, 185 cm, 70 kg) was asked to walk naturally while the left foot and lower leg motion and ground reaction forces were recorded as detailed below. The subject's natural gait cadence was measured as 92 steps/minute, and five trials were conducted at this cadence. Five more trials were run at a higher cadence (112 steps/minute) and a lower cadence (72 steps/minute). The gait cadence was enforced using a metronome.

Motion was recorded using Optotrak active markers (Certus. NDI, Waterloo, ON, Canada). Motion data was collected at 128 Hz. One marker cluster was placed on the foot, one marker cluster on the shank, one marker on the first toe, and one on the fourth and fifth toes (which were taped together in order to secure the marker) as shown in Figure 5.6.

Figure 5.6: Marker placement on the foot

During a standing calibration trial, the following markers were placed and recorded relative to the foot cluster: the lateral and medial malleoli, the heel (posterior protrusion of the calcaneus), the distal heads of metatarsal 1, 3, and 5, and the 1st, 3rd, and 5th toes. These additional markers were used to locate the toe joint and align the test frame axis.

Ground reaction forces and pressures were measured using an AMTI force place (OR6-7. Watertown, MA, USA) and Tekscan pressure mat (Medical Sensor 3005E for F-Scan system. South Boston, MA, USA). Force and moment measurements were collected at 1024 Hz and pressure measurements at 64 Hz. The force and moment measures were later down-sampled to 128 Hz during processing and model optimisation to match the sampling rate of the motion measurements. The force plate and pressure mat locations were measured relative to the Optotrak frame of reference. This allowed the foot position (measured by the motion capture) to be compared with centre of pressure (COP) (measured by the force plate and pressure mat).

To reduce noise, the motion data was filtered with a low-pass filter designed and implemented in Matlab (a dual-pass Butterworth low-pass filter, with the passband at 5 Hz and stopband at 20 Hz with 10 times attenuation).

Frame definitions

The global frame was set so that the Z-axis pointed vertically up, the Y-axis pointed in the direction of movement (anterior), and the X-axis pointed to the right (medial, for the left foot).

The foot frame origin was placed at the heel of the foot with the y_{foot}-axis passing though the 3rd metatarsal and the 1st metatarsal located in the x_{foot}-y_{foot} plane (Figure 5.7).
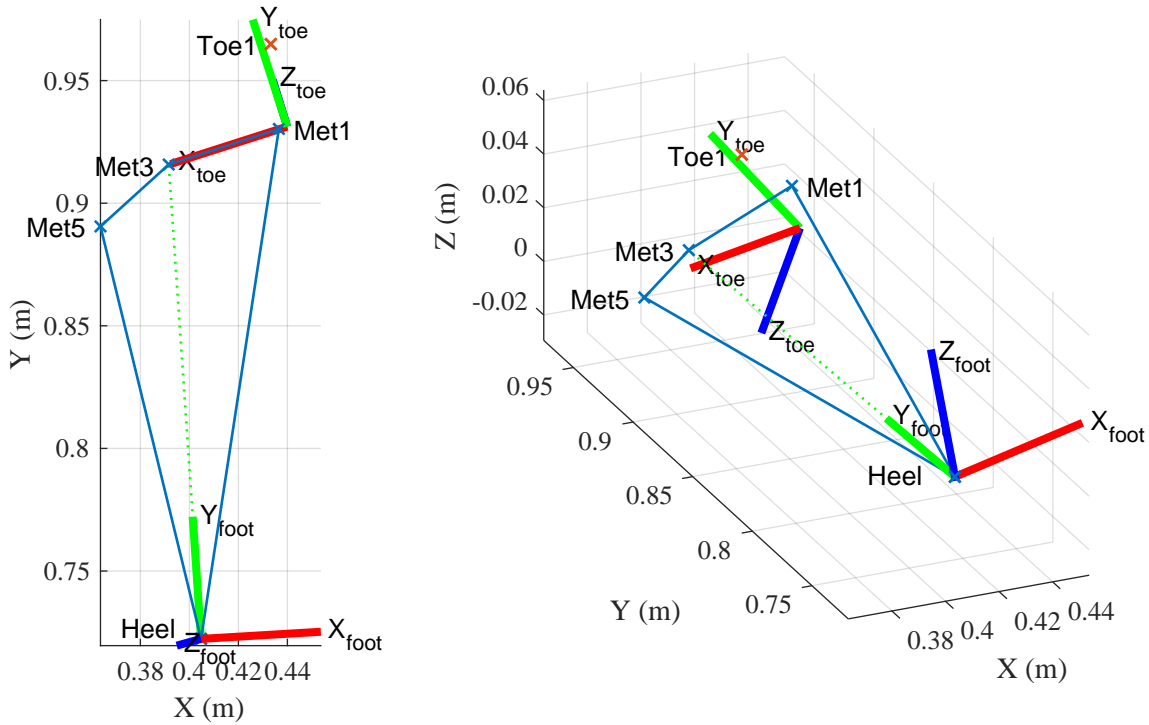
Figure 5.7: Foot and toe frame conventions (shown in global lab frame)

The toe frame was determined using the metatarsal markers and toe marker, with the x_{toe}-axis specifying the axis of revolution for the toe joint. The origin was placed directly below the 1st metatarsal with the x_{toe}-axis parallel to the ground and passing under the 3rd metatarsal. The x_{toe}-axis was placed 16 mm above the ground (16 mm was about half the height of the 3rd metatarsal). The frame was rotated about the x_{toe}-axis so that the toe marker (Toe1) was in the x_{toe}-y_{toe} plane. The position of the toe frame origin with respect to the foot frame is given in Table 5.2.

Table 5.2: Toe frame position

Toe frame origin	(46.8, 205.9, -17.1) mm
Toe frame rotation (1-2-3 body-fixed Euler angles)	2.72, -0.20, -2.89 rad

Toe rotation and rigid body assumption

The original intent was to determine the toe joint rotation from the experimental data, but this proved unreliable. When the two-body foot model was fitted to the experimental data, physiologically impossible toe motion was observed—presumably due to errors in determining the toe axis location during movement. These errors were likely caused by the rigid body assumption for the foot. Only one marker cluster was used to determine the foot location, and this was placed near the proximal end of the foot (Figure 5.6). Internal movement of the foot (i.e. relative movement of the bones that make up the foot) would not have been captured by this marker cluster, so any internal movement resulted in errors which were largest near the distal end of the foot (such as the toe axis).

Due to the errors noted in the experimentally determined toe movement, the rotation was not calculated from the experiment. For the inverse dynamics study (described later) this rotation was determined purely by optimisation.

For the purposes of simplification of the model, the rigid body assumption was kept.

It would be useful in future research to avoid some of these errors. Some possible solutions include placing markers at the proximal and distal ends of the foot, so a better approximation of the true foot location can be found, using stick markers (that is, small motion capture markers attached to the foot via short rigid bars) to help determine the orientation of certain parts of the foot, and using more rigid bodies to represent the foot (this would require more markers to determine the motion of each separate segment). Several studies have recommended more rigid bodies to represent the foot motion, such as Wrbaškić et al. who recommended an additional joint at the anterior talus to better fit experimental movement [90].

Technical problems

Several problems were noted after the completion of the experiment and data collection.

The pressure mat had been set to a higher sensitivity, meaning that some of the measurements hit the maximum saturation limit. It had also been noted that the pressure mat appeared to have a slow response time (well over a second). As a result, the pressure mat predicted a much lower total force than the force plate (Figure 5.8). To partially solve this, the measurements from the pressure mat were scaled such that the total force was equal to that measured by the force plate and less weight was given to the pressure measurements in the optimisation.

When determining the location of the force plate and pressure mat, the Optotrak marker wand was run with an incorrect calibration, rendering the measured positions mostly useless. However, the global origin had been set correctly to a known position in the lab, so the location of the force plate was measured by hand after this mistake was detected. The pressure mat location on the force plate was determined by matching the COP location measured by the pressure mat and the force plate. Note that the remainder of the motion calibration was done correctly; only the measured positions of the pressure mat and force plate had errors.
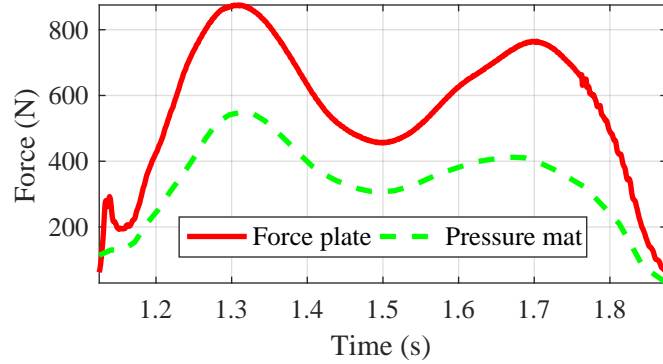
Figure 5.8: Force measured by force plate and pressure mat

5.3.2 Parameter Optimisation Method

To test the model, it was subject to the same motion recorded in the gait experiment (in an inverse dynamic simulation) and the simulated ground reaction forces and pressure were compared to the experimental results.

The reader is reminded that the parameters adjusted by the optimisation method are in Table 5.1.

Toe rotation and motion correction

Since the toe rotation could not be determined experimentally, the toe rotation was determined by optimisation. The rotation angle versus time graph was represented by a cubic spline, and the spline data points were included as parameters in the optimisation

In order to reduce the effect of errors introduced by the rigid body assumption and skin movement, the optimiser was also allowed to adjust the foot motion and orientation. This correction was also specified as a cubic spline, limited to ± 2 mm (for translation in each of the coordinate axes) and ± 0.05 rad (for each of the three rotations).

As mentioned previously, there were some errors in the calculation of the foot motion; this error was largest near toe-off. One effect noted during the inverse dynamics simulation was that the toe slid laterally just before toe-off due to an apparent rotation of the foot. To allow the motion adjustment to correct this error, the lower limit for the z rotation correction was adjusted to -0.3 rad.

The toe rotation and motion correction splines were parametrised by 10 data points evenly spaced over the time of contact. This introduced another 70 parameters (for 3 position correction splines, 3 rotation correction splines, and 1 toe rotation spline) for a total of 100 parameters (including the 30 for the contact model).

Cost function

The optimisation cost function was defined as the mean-square difference between the simulation and experimental results for the normal force, COP location, frictional force, spinning friction, and pressure.

$$
\begin{aligned}
C = & \frac{w_{normal} s_{normal}}{N} \sum (F_{z\ exp} - F_{z\ sim})^2 + \\
& \frac{w_{friction} s_{friction}}{N} \sum \left((F_{x\ exp} - F_{x\ sim})^2 + (F_{y\ exp} - F_{y\ sim})^2 \right) + \\
& \frac{w_{cop} s_{cop}}{N} \sum \left((x_{cop\ exp} - x_{cop\ sim})^2 + (y_{cop\ exp} - y_{cop\ sim})^2 \right) + \\
& \frac{w_{pressure} s_{pressure}}{N} \sum \left[A_{sensor} \sum_x \sum_y |p_{xy\ exp} - p_{xy\ sim}| \right]^2 + \\
& \frac{w_{spin} s_{spin}}{N} \sum (m_{z\ exp} - m_{z\ sim})^2
\end{aligned}
\tag{5.52}
$$

where F_z is the normal force, F_x and F_y are the two lateral forces, x_{cop} and y_{cop} are the coordinates of the COP, p_{xy} is the pressure at point (x, y) on the pressure sensor, A_{sensor} is the area of a single sensor on the pressure mat, m_z is the moment about the vertical z-axis, N is the number of data points, s is a scale factor for each term, and w is a weight for each term. The pressure difference is converted into total force difference (by multiplying the pressure measured at each sensor by the area of the sensor), and is scaled by the same factor as the normal force term. The scale factors are defined in Table 5.3.

Table 5.3: Optimisation function scale factors

$s_i = \frac{1}{M_i^2}$	M_i	Description
s_{normal}	688 N	subject weight
$s_{pressure}$		
$s_{friction}$	$\sqrt{\max\left(F_{x\ exp}^2\right) + \max\left(F_{y\ exp}^2\right)}$	maximum measured friction
s_{cop}	20 cm	COP movement distance
s_{spin}	$\sqrt{\max\left(m_{z\ exp}^2\right)}$	maximum measured spinning friction

The other two moments (m_x and m_y) were not included in the optimisation since they are a function of the COP and normal force which are already included in the optimisation.

Most other similar studies in the literature have only used net force and COP location to optimise the foot model. In this case, pressure distribution was also used in the optimisation, which is expected to improve the model fidelity. However, calculating the pressure distribution was very computationally expensive, compared to the simulation, so the pressure distribution was only calculated at 15 time-frames for each simulation.

During initial tests, the optimisation appeared to only converge to a local minimum. To find a better solution, the initial values were randomly adjusted $\pm 10\%$ several times to find different solutions. Ten different adjustments to the initial conditions in Table 5.4

were used as initial guesses for the optimisation and the best of the solutions was chosen as the optimal solution.

Optimisation was done using a least-squares solver in MATLAB (lsqnonlin) which uses a trust region reflective algorithm.

Some other optimisation methods, such as a simulated annealing algorithm, inherently include some randomness and may remove the need for randomly adjusting the initial conditions. Other methods were not tested in this work.

Root-mean-square error calculation

The relative root-mean-square (RMS) error values (difference between the simulated and experimental values) were calculated in a similar manner to the cost function in Equation (5.52):

$$RMS_{normal} = \frac{1}{M_{normal}} \sqrt{\frac{1}{N} \sum (F_{z\ exp} - F_{z\ sim})^2} \tag{5.53}$$

$$RMS_{friction} = \frac{1}{M_{friction}} \sqrt{\frac{1}{N} \sum \left((F_{x\ exp} - F_{x\ sim})^2 + (F_{y\ exp} - F_{y\ sim})^2\right)} \tag{5.54}$$

$$RMS_{cop} = \frac{1}{M_{cop}} \sqrt{\frac{1}{N} \sum \left((x_{cop\ exp} - x_{cop\ sim})^2 + (y_{cop\ exp} - y_{cop\ sim})^2\right)} \tag{5.55}$$

$$RMS_{pressure} = \frac{1}{M_{pressure}} \sqrt{\frac{1}{N} \sum \left[A_{sensor} \sum_x \sum_y |p_{xy\ exp} - p_{xy\ sim}|\right]^2} \tag{5.56}$$

$$RMS_{spin} = \frac{1}{M_{spin}} \sqrt{\frac{1}{N} \sum (m_{z\ exp} - m_{z\ sim})^2} \tag{5.57}$$

Note that similar to the cost function, the RMS error for pressure was only calculated over 15 time-frames.

The RMS values were scaled by M_i (defined in Table 5.3) to obtain non-dimensional values.

Calibration and validation

The contact model parameters were determined using one gait trial at natural speed using the optimisation method described above (to calibrate the model).

The contact model obtained from the calibration was validated by simulating the other gait trials (at the same cadence and the higher and lower cadences). For the other trials, the toe movement and motion correction needed to be determined by optimisation, but the contact model parameters (the 30 parameters in Table 5.1) were kept the same.

Initial guess

The optimisation required a good initial guess to converge to a reasonable solution. The initial guess used is presented in Table 5.4.

Table 5.4: Contact model parameters for initial guess

	Parameter(s)	Value
Global	k_V	1×10^7 N/m^3
	a_V	-1 s/m
	μ_d	0.1
Heel	a, b, c	30, 50, 30 mm
	r_x, r_y, r_z	0, 30, -15 mm
	α, β, γ	0, 0.15, 0 rad
Ball	a, b, c	60, 30, 30 mm
	r_x, r_y, r_z	10, 170, -13 mm
	α, β, γ	0, 0.2, 0.5 rad
Toe	a, b, c	20, 20, 20 mm
	r_x, r_y, r_z	0, 15, -13 mm
	α, β, γ	0, 0, 0 rad

5.3.3   Results with Friction in Optimisation

The weights for the optimisation function were all set to 1, except for the pressure term ($w_{pressure}$) which was set to 0.1 due to the uncertainties with the pressure measurements (Section 5.3.1). The simulation results for the optimised solution are shown in Figure 5.9 and the RMS errors for this are shown in Table 5.5.

Table 5.5: RMS error for optimised model (including friction in optimisation)

Normal force	Friction force	Spinning friction	COP	Pressure
11.5%	26.5%	14.2%	5.0%	51.7%

The simulated normal force and the COP was similar to the experimental results (11.5% and 5.0% RMS error, respectively). The shape of the pressure profile during gait (only the maximum pressure is shown in the figure, for convenience) had some visual similarities, but shows that the ellipsoids do not match the foot geometry perfectly; the simulated pressure had a 51.7% RMS error, though some of this was from errors in the pressure measurement. The friction forces did not match as well as the normal force did (26.5% RMS error for tangential force, and 14.2% error for spinning friction), though they were of similar magnitudes.

Upon further analysis, it was realised that the simulated friction force and normal force had a very similar trend. This is more visible if the net friction force is shown with the normal force scaled by the coefficient of friction (Figure 5.10).
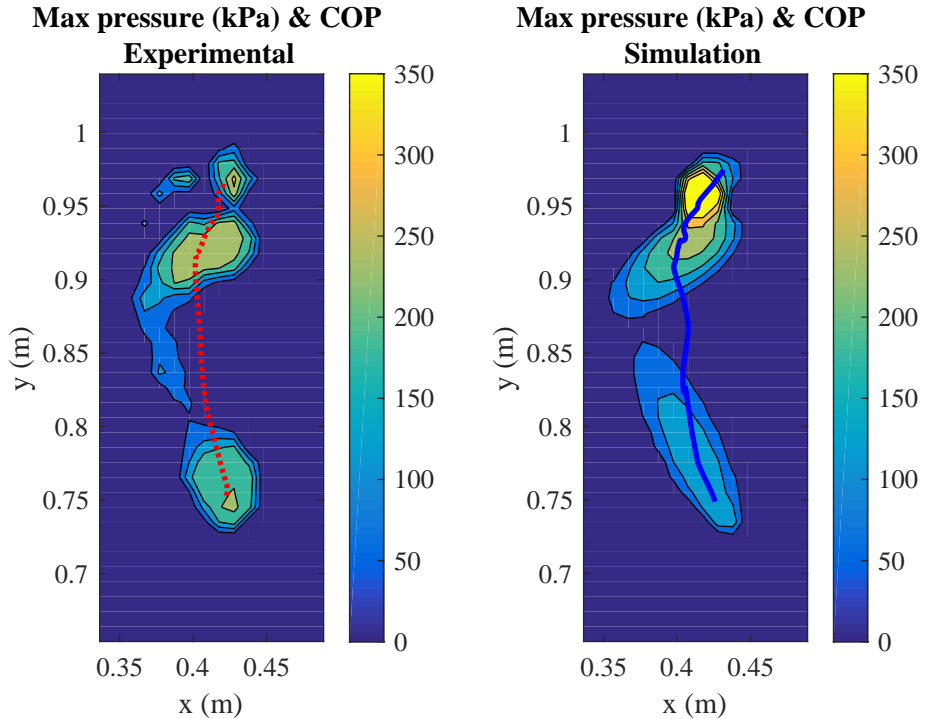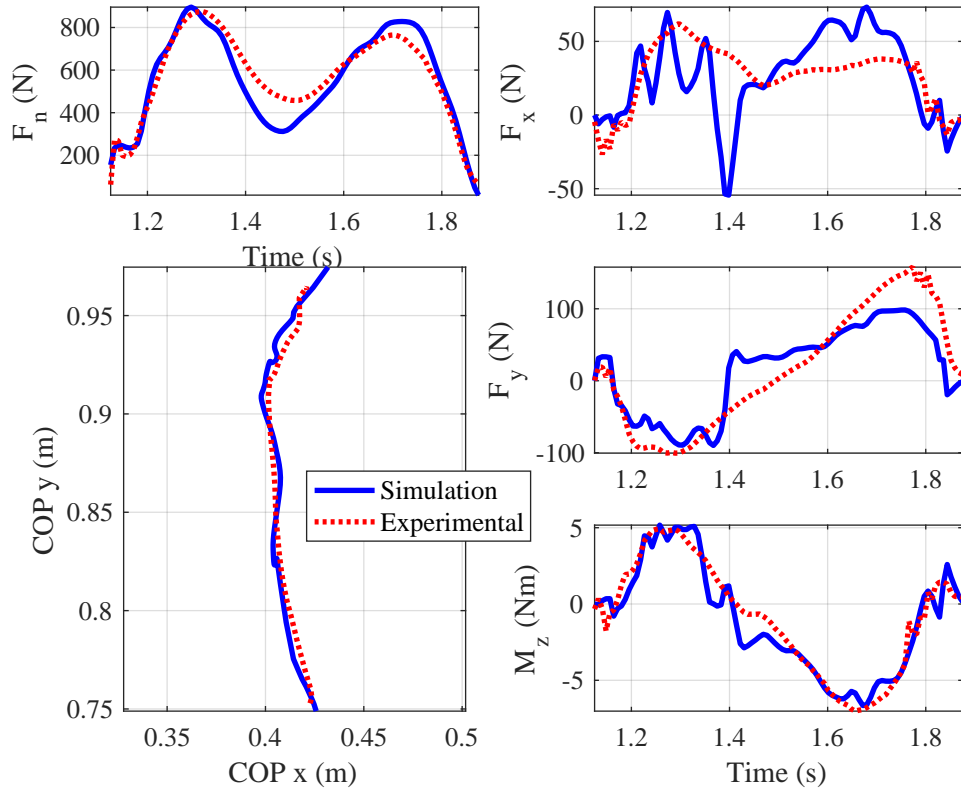
Figure 5.9: Simulated forces (top) and pressures (bottom) for optimal model (with friction)
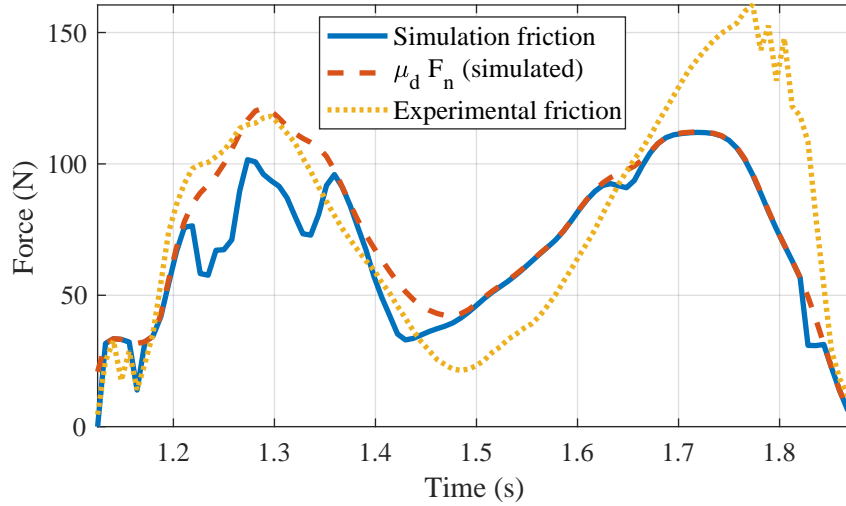
Figure 5.10: Simulated friction, maximum possible friction (based on normal force and $\mu_d F_n$), and experimental friction

In Figure 5.10, the simulated friction values generally follow the shape of the normal force (which dictates the maximum possible value for friction) more closely than the experimental friction values. It may also be noticed in Figure 5.9 that the simulated normal force had a lower minima around $t = 1.45$ s; the optimisation appears to have converged to this so that the friction forces match more closely. The mismatch in friction forces is particularly noticeable near the end of the trial, where the experimental friction peaks to a value much higher than the simulated friction. The friction force was equal to $\mu_s F_n$ for most of the time, which would indicate that the foot was slipping during this time. However, no slipping was noted during the experiment. Also worth noting is that the optimised friction coefficient, $\mu_d = 0.14$, is much lower than expected (Li and Wen measured a coefficient of friction of 0.65 for a bare foot on ceramic tiles [91]).

This difference can be explained as a limitation of using a velocity-based friction model in an inverse-dynamics simulation with little slipping. In the experiment, the foot had little or no slipping; however, it is difficult for a velocity-based friction model to stay in the sticking regime in an inverse simulation. Velocity-based friction models assume that sticking occurs at very small velocities (in this model, less than $v_t = 0.01$ m/s) (Figure 5.11), despite the fact that true sticking would have a velocity of zero. In a forward dynamics simulation, this small level of error in the velocity is generally acceptable. On the other hand, in an inverse dynamics simulation, a small error in the velocity is very likely (from measurement noise or error), which can lead to large changes in the friction force (see force-velocity curve in Figure 5.11). A similar study in the literature is noted to have the same issue: Jackson et al. [80] used a similar method to parametrise a foot-ground contact model with a velocity-based friction model, and obtained a static coefficient of friction of only 0.1. This is particularly surprising since the subject was wearing sports shoes, which should have a higher coefficient of friction in order to provide good grip.

The coefficient of friction obtained in this optimisation was likely the average *required*
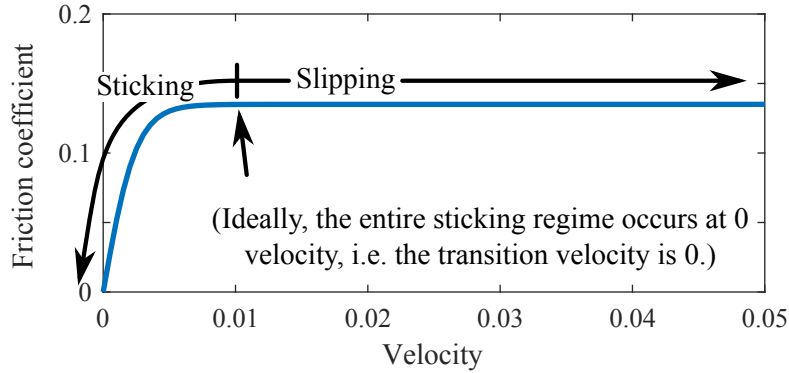
Figure 5.11: Velocity-based friction curve (only dynamic or Coulombic friction)

coefficient of friction. The required coefficient of friction is calculated as the friction force divided by the normal force. Based on other studies, the maximum required coefficient of friction for walking is 0.15 to 0.30 [92], lending plausibility to the theory that the converged value of 0.14 is approximately the average required coefficient of friction for this study.

As a result, friction was ignored in this study. The coefficient of friction would be better identified by a separate experiment, such as dragging the foot across a force plate (such as in [91]). The friction portion of the model would have to be validated using a forward dynamics simulation.

5.3.4   Results without Friction in Optimisation

Calibration results

For the optimisation without friction, the function weights used were $w_{normal} = w_{cop} = 1$, $w_{pressure} = 0.1$, and $w_{friction} = w_{spin} = 0$.

The optimal parameters are shown in Table 5.6, the model geometry is shown in Figure 5.12, and the simulation results are shown in Figure 5.13.

Based on Figure 5.13, the experimental pressure distribution could be improved by the addition of a fourth ellipsoid at the lateral edge of the foot. There is some foot-ground contact along this edge that is unaccounted in the 3-ellipsoid model. However, including a fourth ellipsoid would increase the model complexity and the number of parameters needed for the model.

Validation results

The foot model parametrised in the calibration trial was used to simulate the other trials. The RMS errors for the normal force, COP, and pressure are given in Table 5.7.

With the removal of the friction terms, the normal force matched the experimental results more closely (3.4% RMS error instead of 11.5%). The errors in the COP position and pressure profile also decreased, though not to the same extent.

Table 5.6: Optimised contact model parameters

	Parameter(s)	Value
Global	k_V	1.60×10^7 N/m^3
	a_V	-0.565 s/m
Heel	a, b, c	35.4, 54.0, 22.6 mm
	r_x, r_y, r_z	3.7, 47.9, 0.4 mm
	α, β, γ	0.329, 0.201, 0.101 rad
Ball	a, b, c	63.2, 33.8, 24.0 mm
	r_x, r_y, r_z	20, 167, -0.6 mm
	α, β, γ	-0.235, 0.191, 0.528 rad
Toe	a, b, c	18.2, 18.6, 13.2 mm
	r_x, r_y, r_z	11, 10, -19 mm
	α, β, γ	0.339, 1.23, 0.454 rad
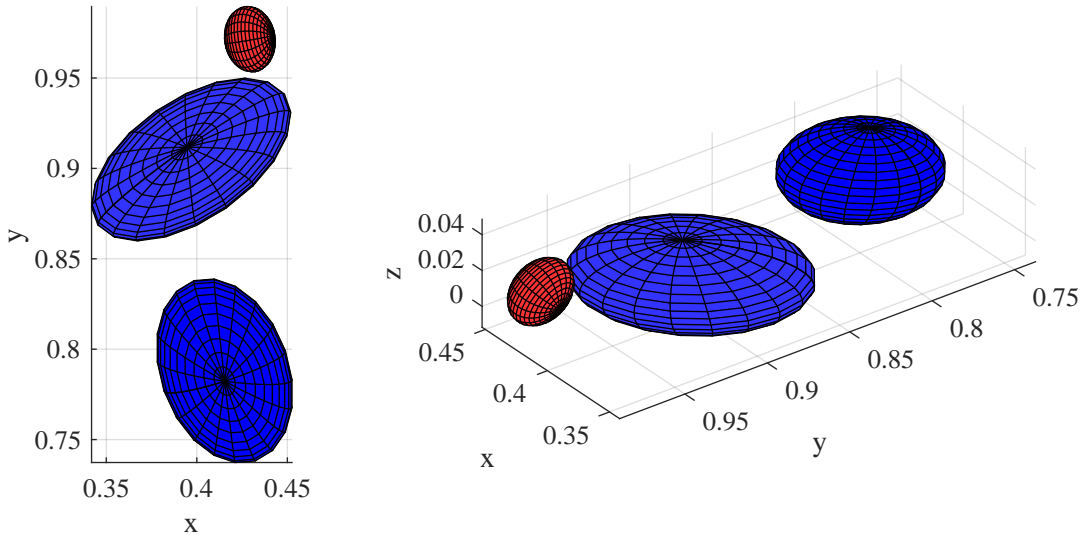
Figure 5.12: Volumetric contact model geometry

Table 5.7: RMS error for foot-ground contact model

Gait cadence (number of trials)	Normal force	COP	Pressure
Calibration: 92 steps/minute (1)	3.4%	3.2%	33.9%
92 steps/minute (3ᵃ)	4.2%	4.2%	38.1%
112 steps/minute (5)	4.9%	6.6%	44.1%
72 steps/minute (4ᵃ)	4.4%	5.0%	40.0%

ᵃ Some trials ignored due to unusual values or processing errors

Figure 5.13: Simulated forces (top) and pressures (bottom) for optimal model (friction was ignored in this simulation)

As would be expected, the calibration trial had the lowest RMS errors, followed by gait trials at the same cadence. The higher cadence trials had the largest RMS values, though none of the trials had very different RMS errors from the calibration trial. The largest difference is between the calibration trial and the high cadence trial COP error, which was doubled. The pressure had the largest erro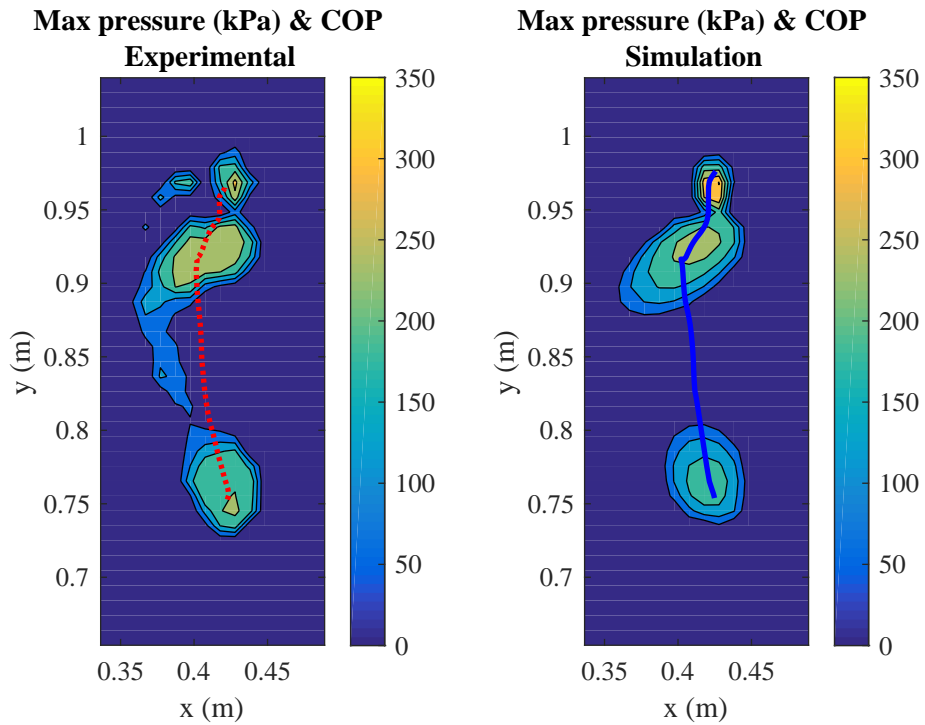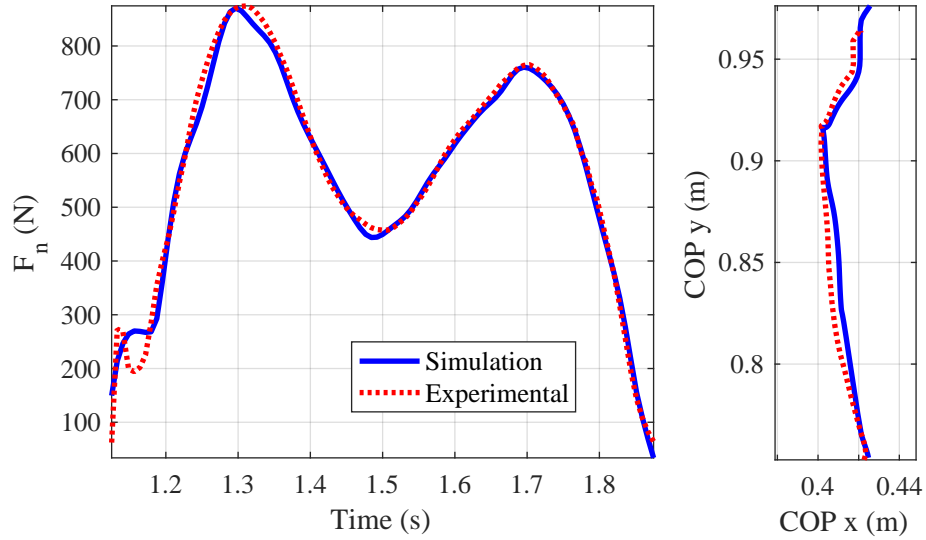rs by almost an order of magnitude. Part of this error would be due to inaccuracies in representing the shape of the plantar surface with simplified shapes and the errors in the pressure measurements.

For comparison, Jackson et al. [80] developed a contact model using similar methods for validation, except that validation was only done using gait at the same cadence. A comparison of the RMS errors for the simulations are given in Table 5.8.

Table 5.8: RMS error comparison with Jackson et al.

| | Normal force (N) | COP (mm) | |
		AP[a]	ML[b]
Volumetric	28.8	8.0	2.4
Jackson et al. [80]	13	25	8

[a] Anterior-posterior direction
[b] Medial-lateral direction

The volumetric model presented here provided much better COP position matching compared to the model of Jackson et al., even for trials at different cadences, but the normal force did not match as closely. Some caution should be taken in comparing the results of these two models, since Jackson et al. used a different method to determine the motion correction and toe flexion and the subjects were of different weights.

5.3.5   Results without Friction or Pressure in Optimisation

Other similar studies in the literature, including Jackson et al. [80], did not use a pressure mat and the pressure data in determining foot parameters. To determine the effect of minimising the pressure errors in the optimisation, the same parameter optimisation was done without minimising pressure errors. For simplicity, only one calibration trial was done to compare the results with those given in Section 5.3.4.

The optimised model geometry is shown in Figure 5.14 and the results from the simulation are in Figure 5.15.

Since the pressure distribution did not need to be calculated in the optimisation, the parameter optimisation took much less computational time: only 10 s, compared to the previous 164 s average. The pressure distribution required calculating the pressure at a large number of points across the contact surface, rather than just the net force and contact location.

The optimised results matched the normal force and centre-of-pressure position more closely, probably because the optimisation was not also attempting to minimise the pressure
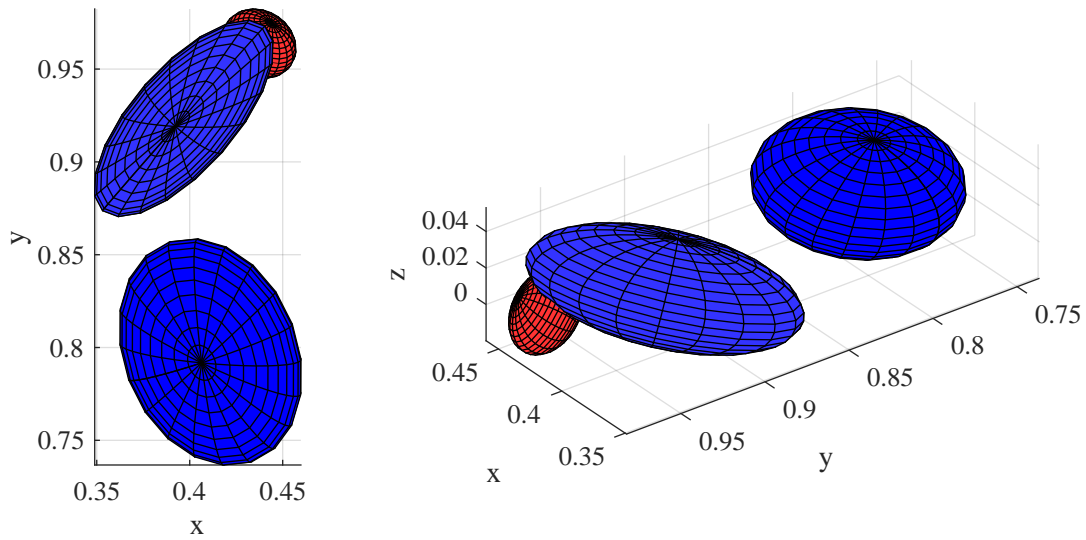
Figure 5.14: Volumetric contact model geometry for optimisation not using pressure distribution

distribution error. However, the resultant pressure distribution is a poor match. The root-mean-square error values for the optimisation with and without considering pressure are given in Table 5.9.

Table 5.9: RMS error for models with and without minimising contact pressure error

Trial Calibration: 92 steps/minute	Normal force	COP	Pressure
With pressure in optimisation	3.4%	3.2%	33.9%
Without pressure in optimisation	2.7%	1.8%	70.2%

The contact model (Figure 5.14) and pressure distribution (Figure 5.15) reveal that the 'toe' contact was placed between the toe and ball of the foot. This presumably happened to match the normal force and COP position more closely, but is an inaccurate representation of the foot geometry.

Also note that the toe rotation was solely determined in the optimisation, so it is uncertain if the "toe" movement here is physiological. The optimisation may have adapted the contact to represents parts of the foot surface other than the toe and converged to non-physiological movement. This problem might be avoided by careful choice of optimisation bounds, but a better solution would be to design an experiment in which the foot movement and toe rotation can be calculated accurately.

Minimising pressure distribution error in the parameter optimisation increases computational time (by at least one order of magnitude) but helps avoid some non-physiological solutions, as presented in this section. It is possible that some of these errors may also have been avoided with a better designed experiment, but it is likely that minimising pressure errors helps converge to more a more accurate model of the foot surface.
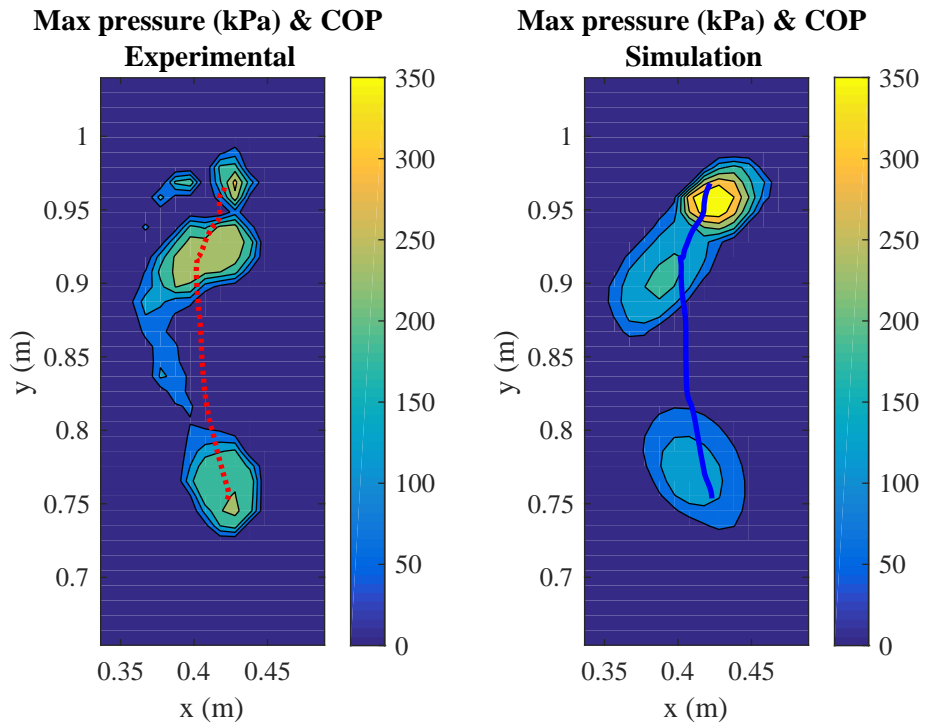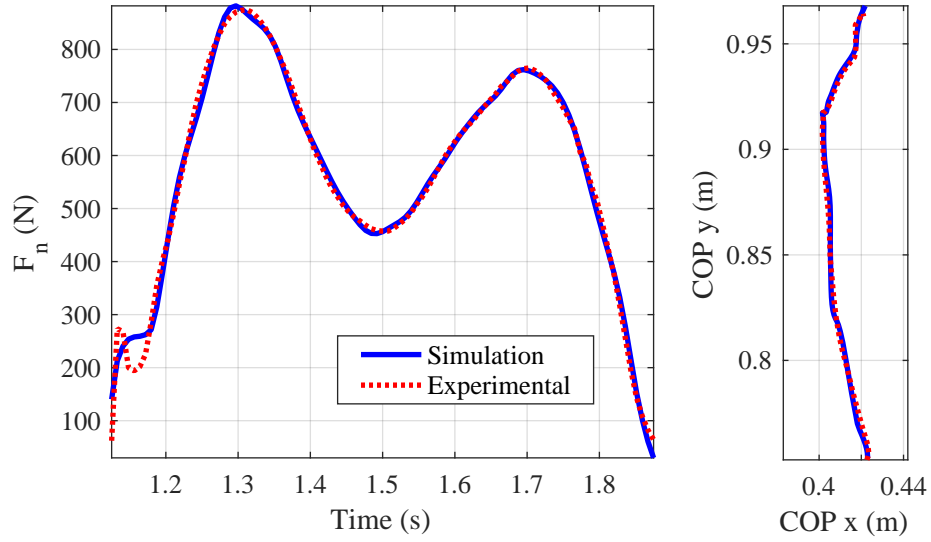
Figure 5.15: Simulated forces (top) and pressures (bottom) for optimisation not using pressure distribution

5.3.6   Computational time

Optimisation was done on a quad-core desktop (Intel® Core™ i7-3770 CPU @ 3.40GHz). Optimisation including friction took 180 s. Optimisations without friction took, on average, 164 s. Just optimising the motion correction for the non-calibration trials took, on average, 82 s. Optimisation without friction or pressure took about 10 s.

The inverse simulation ran over 100 times faster than real-time. However, this does not include calculating the pressure across the contact area, which was used in some of the optimisations. When the simulation was also used to calculate the pressure distribution (at 15 timeframes, on a 39x16 grid), the simulation ran about 15 times faster than real-time.

5.4   Conclusions and Recommendations

5.4.1   Volumetric Contact Model

Analytical equations for volumetric contact between an ellipsoid and a plane were derived and presented. The friction model was adjusted from Gonthier's proposed equations to match more closely with Coulomb friction. In order to keep the equations analytical, the friction model was an approximation that cannot capture all effects, such as perfect sticking or the Contensou effect.

The ellipsoid-plane contact equations were significantly larger and more complex than sphere-plane contact equations.

5.4.2   Experimental Parametrisation and Validation

The developed foot-ground contact model was able to match experimental normal force and COP position within 5% for trials at the same or lower gait cadence. The COP position had higher levels of error for a higher cadence (6.6%). This model has similar accuracy to a recent model using a large number of point contacts [80] (this model has better COP position accuracy, but poorer normal force accuracy).

The foot model ran over 100 times faster than real-time in an inverse simulation (simulation took longer if the pressure distribution was calculated). The parameter optimisation minimising error in normal force, COP position, and pressure took, on average, 164 s.

The model parameter optimisation was sensitive to the initial guess and a good guess was required to converge to the given results. It is uncertain if the provided results are the global minimum, but the developed model was able to closely match the experimental results. As noted by [80], there may be more than one combination of parameters with good prediction results. It is possible that a different optimisation algorithm could improve the results; only one method was used here.

Inverse dynamics simulation and parameter optimisation proved to be an inaccurate method for determining friction parameters and validating the friction model. Unusually

low coefficients of friction were found and the optimisation converged to unusual results (such as adjusting the normal force profile to better match the friction force profile). A different method for determining the coefficient is recommended (such as dragging the foot on a force plate), and the friction model must be validated in a forward dynamics simulation.

The rigid body simplification for the foot introduced inaccuracies when determining foot motion from the gait experiment. In order to continue using this simplification, the optimisation was allowed to apply some motion correction to the experimental data. Using multiple rigid bodies to represent this segment may increase accuracy, but would also increase complexity of the model and the difficulty with parametrisation.

Using additional markers on the foot (particularly near the distal end) or using stick markers may improve accuracy of the motion determined from the experiment, including the toe rotation (such as the experimental method used by [80]). This would hopefully reduce the need for the motion correction introduced in this study.

Results from this study may be improved with a more accurate pressure mat with a faster response time. This would improve the accuracy of the pressure used in the optimisation.

Despite the inaccuracies of the pressure mat, minimising the pressure errors as part of the parameter optimisation appears to result in more accurate model geometry. This comes at a large increase in computational cost in the parameter optimisation. This increased computational cost is only present during parametrisation; the resulting models are equivalent in terms of computational cost. The increased optimisation time comes with the benefit of converging to a more physiological solution, though it may not always be necessary.

The model parameters given here are based on a single subject and a single activity and may not be generalisable. Using several activities to parametrise the model (walking, jumping, and running, etc.) may help improve the model accuracy for a generalised movement. Only using a single subject may be beneficial, however, since subject-specific contact models tend to improve accuracy [60], [61].

Chapter 6

Conclusions and Recommendations

6.1   Conclusions

This thesis presents the use of volumetric contact in multibody dynamics in two novel models: a 3D knee model and foot-ground contact model. Additionally, a friction model for multibody simulation and optimisation was developed and presented.

Knee model

A simple volumetric-contact based knee model was created, based on another knee model in literature. The tibiofemoral contact was modelled as a sphere-on-plane volumetric contact model. In a forward-dynamics simulation, the knee model ran faster than real-time and gave similar contact forces to the model it was based on. The ligament forces did not match as closely, possibly due to slight differences in ligament positions or slack length. Since the results were not compared against any experimental results, it is difficult to comment on the accuracy of this model. This model confirms as a proof-of-concept that volumetric contact can work as a real-time contact model for the knee joint.

Friction model

As a part of developing contact models, friction is also of interest and a lack of a simple, continuous friction model was identified. A novel, continuous, velocity-based friction model was presented to fulfil this need. The friction model was designed to use a minimum number of parameters (5 with viscous friction, or 3 without) for capturing the effects of dynamic friction, stiction, and viscous friction. The proposed model avoids any discontinuities in the system equations and is of similar efficiency to other current velocity-based models, making it well suited for optimisation, sensitivity analysis, and multibody simulation applications.

Foot-ground contact model

A foot-ground contact model was also developed using volumetric contact. Ellipsoid-plane volumetric equations were derived in order to use ellipsoids to represent the contact surface. The volumetric friction model was adjusted to better match Coulombic friction using the friction model described in this thesis. The foot was made of two rigid bodies with one degree of freedom at the toe joint. Three ellipsoids were used to represent the contact surface.

This model was parametrised and validated in an inverse dynamics optimisation to match experimental gait data. Testing against experimental gait data at higher and lower gait cadences demonstrated that the model was able to replicate reaction forces within 7% of experimental values, with the simulation running over 100 times faster than real-time.

It was noted that including a pressure term in the optimisation (to minimise difference between pressure mat readings and simulated pressure) increased the optimisation time significantly, but helped converge to a more physiological solution.

In the parametrisation of the foot-ground contact model it was discovered that inverse-dynamics could not be used to determine friction parameters. As a result, friction was not included in the current model.

Volumetric contact in biomechanics

Two contact models for use in multibody biomechanics simulation have been developed using volumetric contact. These models are computationally efficient, able to run faster than real-time for use in optimisations, and were produce results similar to experimental results or results in the literature.

Accurate geometry for the contact surfaces is very important, so good medical images or parameter optimisation is necessary.

An advantage of volumetric contact is that it can be used to calculate the contact pressure distribution over a contact surface (such as done in the foot-ground contact model). This gives the same data that a pressure mat at the contact surface would give, and provides more insight into the contact forces than most current models of similar computational efficiency.

6.2   Recommendations

Volumetric knee model

Since the knee model was only developed as a proof-of-concept and was only based on one other model in the literature, it could be improved in several ways, such as

- using geometry based on updated medical images of contact geometry (especially if developing a subject-specific model),

- using better fitting geometry for volumetric contact (ellipsoid-plane contact equations were derived in this thesis but not used in the knee model),

- including muscles in the model,

- and including the effects of the ligaments and muscles wrapping around the bone (such as the patella for the quadriceps wrapping).

Limited validation of the model has been done to this point, so a more complete validation of the model would also be useful. Possible future steps include:

- using the knee model as a part in a complete human body model,

- and simulating several different load-bearing activities of the knee.

Volumetric foot-ground contact model

Motion tracking markers should be spread across the foot in order to better determine foot movement. Poorly placed markers and unaccounted flexibility of the foot introduced large errors in determining the toe joint location in this study. Stick markers could also be used to improve the accuracy of orientation measurements.

Additionally, the pressure mat used in this experiment had poor accuracy, probably due to slow response time. A pressure mat with higher accuracy and shorter response time would improve measurements and may improve the parameter optimisation.

The contact model accuracy could probably be improved by using more rigid segments, using a larger number of contact shapes, or using more complex shapes that better match the foot. However, this would also increase model complexity, so a balance is needed.

Using several experiments with different types of movements to parametrise the foot model may make a more generalisable model.

Other optimisation methods should be explored to determine what method is best suited for this parametrisation problem.

The friction model has not been validated. Friction would be better parametrised using an experiment that includes slipping of the foot, such as a subject sliding his or her feet on a force plate. Validation of the model would have to be done using a forward dynamics simulation.

References

[1] J. A. C. Ambrósio and A. Kecskeméthy, "Multibody dynamics of biomechanical models for human motion via optimization," in *Multibody Dynamics: Computational Methods and Applications*, J. C. García Orden, J. M. Goicolea, and J. Cuadrado, Eds., Dordrecht: Springer Netherlands, 2007, pp. 245–272.

[2] J. A. Thompson, M. W. Hast, J. F. Granger, S. J. Piazza, and R. A. Siston, "Biomechanical effects of total knee arthroplasty component malrotation: A computational simulation," *Journal of Orthopaedic Research*, vol. 29, no. 7, pp. 969–975, 2011.

[3] C. R. Smith, M. F. Vignos, R. L. Lenhart, J. Kaiser, and D. G. Thelen, "The influence of component alignment and ligament properties on tibiofemoral contact forces in total knee replacement," *ASME Journal of Biomechanical Engineering*, vol. 138, no. 2, 021017:1–10, 2016.

[4] F. C. Anderson and M. G. Pandy, "Dynamic optimization of human walking," *ASME Journal of Biomechanical Engineering*, vol. 123, no. 5, pp. 381–390, 2001.

[5] M. Peasgood, E. Kubica, and J. McPhee, "Stabilization of a dynamic walking gait simulation," *ASME Journal of Computational and Nonlinear Dynamics*, vol. 2, no. 1, pp. 65–72, 2007.

[6] B. J. Fregly, J. A. Reinbolt, K. L. Rooney, K. H. Mitchell, and T. L. Chmielewski, "Design of patient-specific gait modifications for knee osteoarthritis rehabilitation," *IEEE Transactions on Biomedical Engineering*, vol. 54, no. 9, pp. 1687–1695, 2007.

[7] S. J. Allen, M. A. King, and M. R. Yeadon, "Optimisation of phase ratio in the triple jump using computer simulation," *Human Movement Science*, vol. 46, pp. 167–176, 2016.

[8] J. P. Halloran, M. Ackermann, A. Erdemir, and A. J. van den Bogert, "Concurrent musculoskeletal dynamics and finite element analysis predicts altered gait patterns to reduce foot tissue loading," *Journal of Biomechanics*, vol. 43, no. 14, pp. 2810–2815, 2010.

[9] Y. Gonthier, J. McPhee, C. Lange, and J.-C. Piedbœuf, "A contact modeling method based on volumetric properties," in *ASME IDETC*, Long Beach, California, USA, 2005, pp. 477–486.

[10] M. Sharif Shourijeh and J. McPhee, "Efficient hyper-volumetric contact dynamic modelling of the foot within human gait simulations," in *ASME IDETC*, Portland, Oregon, USA, 2013.

[11] P. Brown and J. McPhee, "A continuous velocity-based friction model for dynamics and control with physically meaningful parameters," *ASME Journal of Computational and Nonlinear Dynamics*, vol. 11, no. 5, 054502:1–6, 2016.

[12] A. Seth and M. G. Pandy, "A neuromusculoskeletal tracking method for estimating individual muscle forces in human movement," *Journal of Biomechanics*, vol. 40, no. 2, pp. 356–366, 2007.

[13] E. J. Berger, "Friction modeling for dynamic system simulation," *Applied Mechanics Reviews*, vol. 55, no. 6, pp. 535–577, 2002.

[14] J. M. Banerjee and J. McPhee, "Graph-theoretic sensitivity analysis of multibody systems," *ASME Journal of Computational and Nonlinear Dynamics*, vol. 9, no. 4, 041009:1–8, 2014.

[15] G. Gilardi and I. Sharf, "Literature survey of contact dynamics modelling," *Mechanism and Machine Theory*, vol. 37, no. 10, pp. 1213–1239, 2002.

[16] K. H. Hunt and F. R. E. Crossley, "Coefficient of restitution interpreted as damping in vibroimpact," *ASME Journal of Applied Mechanics*, vol. 42, no. 2, pp. 440–445, 1975.

[17] K. L. Johnson, *Contact mechanics*. Cambridge: Cambridge University Press, 1985.

[18] P. Flores, "Compliant contact force approach for forward dynamic modeling and analysis of biomechanical systems," *Procedia IUTAM*, vol. 2, pp. 58–67, 2011.

[19] P. Flores, M. Machado, M. T. Silva, and J. M. Martins, "On the continuous contact force models for soft materials in multibody dynamics," *Multibody System Dynamics*, vol. 25, no. 3, pp. 357–375, 2011.

[20] Y. Gonthier, J. McPhee, C. Lange, and J.-C. Piedbœuf, "A regularized contact model with asymmetric damping and dwell-time dependent friction," *Multibody System Dynamics*, vol. 11, no. 3, pp. 209–233, 2004.

[21] D. S. Lopes, R. R. Neptune, J. A. Ambrósio, and M. T. Silva, "A superellipsoid-plane model for simulating foot-ground contact during human gait," *Computer Methods in Biomechanics and Biomedical Engineering*, pp. 1–10, 2015.

[22] M. Millard and A. Kecskeméthy, "A 3D foot-ground model using disk contacts," in *The 3rd Joint International Conference on Multibody System Dynamics & The 7th Asian Conference on Multibody Dynamics*, Busan, Korea, 2014.

[23] A. Zmitrowicz, "Contact stresses: A short survey of models and methods of computations," *Archive of Applied Mechanics*, vol. 80, no. 12, pp. 1407–1428, 2010.

[24] A. Pérez-González, C. Fenollosa-Esteve, J. L. Sancho-Bru, F. T. Sánchez-Marín, M. Vergara, and P. J. Rodríguez-Cervantes, "A modified elastic foundation contact model for application in 3D models of the prosthetic knee," *Medical Engineering and Physics*, vol. 30, no. 3, pp. 387–398, 2008.

[25] B. J. Fregly, Y. Bei, and M. E. Sylvester, "Experimental evaluation of an elastic foundation model to predict contact pressures in knee replacements," *Journal of Biomechanics*, vol. 36, no. 11, pp. 1659–1668, 2003.

[26] Y.-C. Lin, R. T. Haftka, N. V. Queipo, and B. J. Fregly, "Surrogate articular contact models for computationally efficient multibody dynamic simulations," *Medical Engineering and Physics*, vol. 32, no. 6, pp. 584–594, 2010.

[27] I. Eskinazi and B. J. Fregly, "Surrogate modeling of deformable joint contact using artificial neural networks," *Medical Engineering and Physics*, vol. 37, no. 9, pp. 885–891, 2015.

[28] M. Boos and J. McPhee, "Volumetric modeling and experimental validation of normal contact dynamic forces," *ASME Journal of Computational and Nonlinear Dynamics*, vol. 8, no. 2, 021006:1–8, 2013.

[29] Y. Gonthier, "Contact dynamics modelling for robotic task simulation," PhD Thesis, University of Waterloo, 2007.

[30] T. K. Uchida, M. A. Sherman, and S. L. Delp, "Making a meaningful impact: Modelling simultaneous frictional collisions in spatial multibody systems," *Proceedings of the Royal Society A*, vol. 471, no. 20140859, 2015.

[31] J. Fleischmann, R. Serban, D. Negrut, and P. Jayakumar, "On the importance of displacement history in soft-body contact models," *ASME Journal of Computational and Nonlinear Dynamics*, vol. 11, no. 4, 044502:1–5, 2016.

[32] J. Liang, S. Fillmore, and O. Ma, "An extended bristle friction force model with experimental validation," *Mechanism and Machine Theory*, vol. 56, pp. 123–137, 2012.

[33] S. Andersson, A. Söderberg, and S. Björklund, "Friction models for sliding dry, boundary and mixed lubricated contacts," *Tribology International*, vol. 40, no. 4, pp. 580–587, 2007.

[34] C. Canudas de Wit, H. Olsson, K. J. Aström, and P. Lischinsky, "A new model for control of systems with friction," *IEEE Transactions on Automatic Control*, vol. 40, no. 3, pp. 419–425, 1995.

[35] B. K. Madeti, S. R. Chalamalasetti, and S. K. S. siva rao Bolla Pragada, "Biomechanics of knee joint — a review," *Frontiers of Mechanical Engineering*, vol. 10, no. 2, pp. 176–186, 2015.

[36] M. S. Hefzy and E. S. Grood, "Review of knee models," *Applied Mechanics Reviews*, vol. 41, no. 1, pp. 1–13, 1988.

[37] M. S. Hefzy and T. D. V. Cooke, "Review of knee models: 1996 update," *Applied Mechanics Reviews*, vol. 49, no. 10S, S187–S193, 1996.

[38] M. Sharif Shourijeh and J. McPhee, "Forward dynamic optimization of human gait simulations: A global parameterization approach," *ASME Journal of Computational and Nonlinear Dynamics*, vol. 9, no. 3, 031018:1–11, 2014.

[39] F. Mouzo, U. Lugrís, R. Pàmies-Vilà, J. M. Font-Llagunes, and J. Cuadrado, "Under-actuated approach for the control-based forward dynamic analysis of acquired gait motions," in *ECCOMAS Thematic Conference on Multibody Dynamics*, Barcelona, Catalonia, Spain, 2015.

[40] R. Di Gregorio, V. Parenti-Castelli, J. J. O'Connor, and A. Leardini, "Mathematical models of passive motion at the human ankle joint by equivalent spatial parallel mechanisms," *Medical & Biological Engineering & Computing*, vol. 45, no. 3, pp. 305–313, 2007.

[41] A. Hall, "Formulation of a path-following joint for multibody system dynamics," PhD Thesis, University of Waterloo, 2015.

[42] E. M. Abdel-Rahman and M. S. Hefzy, "A two-dimensional dynamic anatomical model of the human knee joint," *ASME Journal of Biomechanical Engineering*, vol. 115, no. 4A, pp. 357–365, 1993.

[43] ——, "Three-dimensional dynamic behaviour of the human knee joint under impact loading," *Medical Engineering and Physics*, vol. 20, no. 4, pp. 276–290, 1998.

[44] S. J. Piazza and S. L. Delp, "Three-dimensional dynamic simulation of total knee replacement motion during a step-up task," *ASME Journal of Biomechanical Engineering*, vol. 123, no. 6, pp. 599–606, 2001.

[45] S. Bersini, V. Sansone, and C. A. Frigo, "A dynamic multibody model of the physiological knee to predict internal loads during movement in gravitational field," *Computer Methods in Biomechanics and Biomedical Engineering*, vol. 19, no. 5, pp. 571–579, 2016.

[46] L. Blankevoort, J. H. Kuiper, R. Huiskes, and H. J. Grootenboer, "Articular contact in a three-dimensional model of the knee," *Journal of Biomechanics*, vol. 24, no. 11, pp. 1019–1031, 1991.

[47] G. Serrancolí, A. L. Kinney, B. J. Fregly, and J. M. Font-Llagunes, "The influence of neuromusculoskeletal model calibration method on predicted knee contact forces during walking," in *ECCOMAS Thematic Conference on Multibody Dynamics*, Barcelona, Catalonia, Spain: Centre Internacional de Mètodes Numèrics en Enginyeria, 2015, pp. 1068–1079.

[48] B. Beynnon, J. Yu, D. Huston, B. Fleming, R. Johnson, L. Haugh, and M. H. Pope, "A sagittal plane model of the knee and cruciate ligaments with application of a sensitivity analysis," *ASME Journal of Biomechanical Engineering*, vol. 118, no. 2, pp. 227–239, 1996.

[49] K. B. Shelburne and M. G. Pandy, "A musculoskeletal model of the knee for evaluating ligament forces during isometric contractions," *Journal of Biomechanics*, vol. 30, no. 2, pp. 163–176, 1997.

[50] A. E. Engin and M. H. Moeinzadeh, "Dynamic modelling of human articulating joints," *Mathematical Modelling*, vol. 4, no. 2, pp. 117–141, 1983.

[51] A. E. Engin and S. T. Tümer, "Improved dynamic model of the human knee joint and its response to impact loading on the lower leg," *ASME Journal of Biomechanical Engineering*, vol. 115, no. 2, pp. 137–143, 1993.

[52] M. Machado, P. Flores, J. C. P. Claro, J. Ambrósio, M. Silva, A. Completo, and H. M. Lankarani, "Development of a planar multibody model of the human knee joint," *Nonlinear Dynamics*, vol. 60, no. 3, pp. 459–478, 2010.

[53] B. J. Fregly, T. F. Besier, D. G. Lloyd, S. L. Delp, S. A. Banks, M. G. Pandy, and D. D. D'Lima, "Grand challenge competition to predict in vivo knee loads," *Journal of Orthopaedic Research*, vol. 30, no. 4, pp. 503–513, 2012.

[54] J. R. Essinger, P. F. Leyvraz, J. H. Heegard, and D. D. Robertson, "A mathematical model for the evaluation of the behaviour during flexion of condylar-type knee prostheses," *Journal of Biomechanics*, vol. 22, no. 11-12, pp. 1229–1241, 1989.

[55] M. G. Pandy, K. Sasaki, and S. Kim, "A three-dimensional musculoskeletal model of the human knee joint. part 1: Theoretical construction," *Computer Methods in Biomechanics and Biomedical Engineering*, vol. 1, no. 2, pp. 87–108, 1997.

[56] I. Argatov, "Development of an asymptotic modeling methodology for tibio-femoral contact in multibody dynamic simulations of the human knee joint," *Multibody System Dynamics*, vol. 28, no. 1, pp. 3–20, 2011.

[57] Y. Bei and B. J. Fregly, "Multibody dynamic simulation of knee contact mechanics," *Medical Engineering and Physics*, vol. 26, no. 9, pp. 777–789, 2004.

[58] L. E. DeFrate, H. Sun, T. J. Gill, H. E. Rubash, and G. Li, "In vivo tibiofemoral contact analysis using 3D MRI-based knee models," *Journal of Biomechanics*, vol. 37, no. 10, pp. 1499–1504, 2004.

[59] J. Wismans, F. Veldpaus, J. Janssen, A. Huson, and P. Struben, "A three-dimensional mathematical of the knee-joint," *Journal of Biomechanics*, vol. 13, no. 8, pp. 677–685, 1980.

[60] P. Gerus, M. Sartori, T. F. Besier, B. J. Fregly, S. L. Delp, S. A. Banks, M. G. Pandy, D. D. D'Lima, and D. G. Lloyd, "Subject-specific knee joint geometry improves predictions of medial tibiofemoral contact forces," *Journal of Biomechanics*, vol. 46, no. 16, pp. 2778–2786, 2013.

[61] M. Wesseling, F. De Groote, L. Bosmans, W. Bartels, C. Meyer, K. Desloovere, and I. Jonkers, "Subject-specific geometrical detail rather than cost function formulation affects hip loading calculation," *Computer Methods in Biomechanics and Biomedical Engineering*, vol. 19, no. 14, pp. 1475–1488, 2016.

[62] T. J. A. Momersteeg, L. Blankevoort, R. Huiskes, J. G. M. Kooloos, J. M. G. Kauer, and J. C. M. Hendriks, "The effect of variable relative insertion orientation of human knee bone-ligament-bone complexes on the tensile stiffness," *Journal of Biomechanics*, vol. 28, no. 6, pp. 745–752, 1995.

[63] T. J. Mommersteeg, L. Blankevoort, R. Huiskes, J. G. Kooloos, and J. M. Kauer, "Characterization of the mechanical behavior of human knee ligaments: A numerical-experimental approach," *Journal of Biomechanics*, vol. 29, no. 2, pp. 151–60, 1996.

[64] H. H. Rachmat, D. Janssen, W. J. Zevenbergen, G. J. Verkerke, R. L. Diercks, and N. Verdonschot, "Generating finite element models of the knee: How accurately can we determine ligament attachment sites from MRI scans?" *Medical Engineering and Physics*, vol. 36, no. 6, pp. 701–707, 2014.

[65] A. Garg and P. S. Walker, "Prediction of total knee motion using a three-dimensional computer-graphics model," *Journal of Biomechanics*, vol. 23, no. 1, pp. 45–58, 1990.

[66] A. Viidik, "A rheological model for uncalcified parallel-fibred collagenous tissue," *Journal of Biomechanics*, vol. 1, no. 1, pp. 3–11, 1968.

[67] A. E. Engin and M. H. Moeinzadeh, "Modeling of human joint structures," AFAMRL, AFAMRL-TR-81-117, Tech. Rep., 1982.

[68] K. L. Moore, A. F. Dalley, and A. M. R. Agur, *Clinically oriented anatomy*, 6th ed. Philadelphia: Lippincott Williams & Wilkins, 2010.

[69] L. Blankevoort and R. Huiskes, "Validation of a three-dimensional model of the knee," *Journal of Biomechanics*, vol. 29, no. 7, pp. 955–961, 1996.

[70] M. G. Pandy and K. Sasaki, "A three-dimensional musculoskeletal model of the human knee joint. part 2: Analysis of ligament function," *Computer Methods in Biomechanics and Biomedical Engineering*, vol. 1, pp. 265–283, 1998.

[71] T. M. Guess, "Forward dynamics simulation using a natural knee with menisci in the multibody framework," *Multibody System Dynamics*, vol. 28, no. 1, pp. 37–53, 2012.

[72] M. Kia, A. P. Stylianou, and T. M. Guess, "Evaluation of a musculoskeletal model with prosthetic knee through six experimental gait trials," *Medical Engineering and Physics*, vol. 36, no. 3, pp. 335–344, 2014.

[73] S. Onyshko and D. A. Winter, "A mathematical model for the dynamics of human locomotion," *Journal of Biomechanics*, vol. 13, no. 4, pp. 361–368, 1980.

[74] S. Siegler, R. Seliktar, and W. Hyman, "Simulation of human gait with the aid of a simple mechanical model," *Journal of Biomechanics*, vol. 15, no. 6, pp. 415–425, 1982.

[75] L. Ren, D. Howard, L. Ren, C. Nester, and L. Tian, "A generic analytical foot rollover model for predicting translational ankle kinematics in gait simulation studies," *Journal of Biomechanics*, vol. 43, no. 2, pp. 194–202, 2010.

[76] A. H. Hansen, D. S. Childress, and E. H. Knox, "Roll-over shapes of human locomotor systems: Effects of walking speed," *Clinical Biomechanics*, vol. 19, no. 4, pp. 407–414, 2004.

[77] L. A. Gilchrist and D. A. Winter, "A two-part, viscoelastic foot model for use in gait simulations," *Journal of Biomechanics*, vol. 29, no. 6, pp. 795–798, 1996.

[78] F. C. Anderson and M. G. Pandy, "A dynamic optimization solution for vertical jumping in three dimensions," *Computer Methods in Biomechanics and Biomedical Engineering*, vol. 2, no. 3, pp. 201–231, 1999.

[79] M. Millard, J. McPhee, and E. Kubica, "Multi-step forward dynamic gait simulation," in *Multibody Dynamics: Computational Methods and Applications*, C. L. Bottasso, Ed., Dordrecht: Springer Netherlands, 2009, pp. 25–43.

[80] J. N. Jackson, C. J. Hass, and B. J. Fregly, "Development of a subject-specific foot-ground contact model for walking," *ASME Journal of Biomechanical Engineering*, vol. 138, no. 9, 091002:1–12, 2016.

[81]   A. Perrier, V. Luboz, M. Bucki, N. Vuillerme, and Y. Payan, "Conception and eval-uation of a 3D musculoskeletal finite element foot model," *Computer Methods in Biomechanics and Biomedical Engineering*, 2015.

[82]   K. Deschamps, F. Staes, P. Roosen, F. Nobels, K. Desloovere, H. Bruyninckx, and G. A. Matricali, "Body of evidence supporting the clinical use of 3D multisegment foot models: A systematic review," *Gait & Posture*, vol. 33, no. 3, pp. 338–349, 2011.

[83]   R. D. Crowninshield and R. A. Brand, "The prediction of forces in joint structures: Distribution of intersegmental resultants," *Exercise and Sport Sciences Reviews*, vol. 9, no. 1, pp. 159–181, 1981.

[84]   M. S. Hefzy and E. M. Abdel-Rahman, "Three-dimensional dynamic anatomical modeling of the human knee joint," in *Biomechanical Systems: Techniques and Applications, Volume III: Musculoskeletal Models and Techniques*, C. T. Leondes, Ed., CRC Press, 2000, ch. 1.

[85]   E. S. Grood and W. J. Suntay, "A joint coordinate system for the clinical description of three-dimensional motions: Application to the knee," *ASME Journal of Biomechanical Engineering*, vol. 105, no. 2, pp. 136–144, 1983.

[86]   Simbody. (Nov. 2016). HuntCrossleyForce class reference, [Online]. Available: `simtk.org/api_docs/simbody/latest/classSimTK_1_1HuntCrossleyForce.html`.

[87]   T. Specker, M. Buchholz, and K. Dietmayer, "A new approach of dynamic friction modelling for simulation and observation," in *Proceedings of the 19th World Congress of The International Federation of Automatic Control, Cape Town, South Africa*, 2014, pp. 4523–4528.

[88]   E. Rabinowicz, "Stick and slip," *Scientific American*, vol. 194, no. 5, pp. 109–118, 1956.

[89]   P. A. Tipler, *Physics for scientists and engineers*, 3rd ed. New York, NY: Worth Publishers, 1991.

[90]   N. Wrbaškić and J. J. Dowling, "An investigation into the deformable characteristics of the human foot using fluoroscopic imaging," *Clinical Biomechanics*, vol. 22, no. 2, pp. 230–238, 2007.

[91]   K. W. Li and H. C. Wen, "Friction between foot and floor under barefoot conditions: A pilot study," *IEEE International Conference on Industrial Engineering and Engineering Management*, pp. 1651–1655, 2014.

[92]   R. Grönqvist, J. Abeysekera, G. Gard, S. M. Hsiang, T. B. Leamon, D. J. Newman, K. Gielo-Perczak, T. E. Lockhart, and C. Y. Pai, "Human-centred approaches in slipperiness measurement," *Ergonomics*, vol. 44, no. 13, pp. 1167–1199, 2001.